Biophysical *Journal*
Article

Biophysical Society

Stochastic model of T cell repolarization during target elimination (II)

Ivan Hornak[1,*] and Heiko Rieger[1]
[1]Department of Theoretical Physics, Center for Biophysics, Saarland University, Saarbrücken, Germany

ABSTRACT Cytotoxic T lymphocytes (T cells) and natural killer cells form a tight contact, the immunological synapse (IS), with target cells, where they release their lytic granules containing perforin/granzyme and cytokine-containing vesicles. During this process the cell repolarizes and moves the microtubule organizing center (MTOC) toward the IS. In the first part of our work we developed a computational model for the molecular-motor-driven motion of the microtubule cytoskeleton during T cell polarization and analyzed the effects of cortical-sliding and capture-shrinkage mechanisms. Here we use this model to analyze the dynamics of the MTOC repositioning in situations in which 1) the IS is in an arbitrary position with respect to the initial position of the MTOC and 2) the T cell has two IS at two arbitrary positions. In the case of one IS, we found that the initial position determines which mechanism is dominant and that the time of repositioning does not rise monotonously with the MTOC-IS distance. In the case of two IS, we observe several scenarios that have also been reported experimentally: the MTOC alternates stochastically (but with a well-defined average transition time) between the two IS; it wiggles in between the two IS without transiting to one of the two; or it is at some point pulled to one of the two IS and stays there. Our model allows one to predict which scenario emerges in dependency of the mechanisms in action and the number of dyneins present. We report that the presence of capture-shrinkage mechanism in at least one IS is necessary to assure the transitions in every cell configuration. Moreover, the frequency of transitions does not decrease with the distance between the two IS and is the highest when both mechanisms are present in both IS.

SIGNIFICANCE Repositioning of the microtubule organizing center (MTOC) plays a key role in the process of target cell elimination of cytotoxic killer cells (T cells and natural killer cells). We use a recently established model for the molecular-motor-driven motion of the MT cytoskeleton confined between the membrane and the nucleus during T cell polarization to make quantitative predictions about the MTOC dynamics and the MT cytoskeleton morphology comparable with experiments. In the presence of two IS it predicts oscillatory, fluctuating, or bistable MTOC dynamics in dependency of the dynein distribution and the action of a cortical-sliding or a capture-shrinkage mechanism, which allows experimental conclusions on the basis of the measurement of MTOC trajectories.

INTRODUCTION

T cells have a key role in the adaptive branch of our immune system by finding and destroying virus-infected and tumor cells, parasites, and foreign invaders. Cytotoxic killing of a target cell is achieved in three subsequent steps. First, the T cell binds to the surface of the target cell and creates a tight contact zone called immunological synapse (IS) (1–9). Second, the T cell relocates the microtubule organizing center (MTOC) toward the IS by a massive movement of the entire microtubule (MT) cytoskeleton due to forces acting on MTs (10–16). This process involves the repositioning of mitochondria, the Golgi apparatus, and the endoplasmic reticulum, since the organelles are bound to the cytoskeleton and relocate with it (14,17–22). In the third step, the T cell releases the cytotoxic material from the lytic granules toward the target cell, leading to its death by necrosis or aphthosis (23–28). The secretion of lytic granules can take place without the MTOC repolarization (29), or before it (30). However, it does not make the repositioning redundant, since the MTOC-accompanied granule secretion may be crucial for the killing of resistant cells.

The IS is divided into several supramolecular activation clusters (SMACs) including ring-shaped peripheral SMAC (pSMAC) (7,9,31–33). Dynein, a minus-end-directed (toward the MTOC) molecular motor protein, is indispensable

Submitted June 28, 2021, and accepted for publication February 16, 2022.
*Correspondence: hornak@lusi.uni-sb.de
Editor: Kevin A. Janes.
https://doi.org/10.1016/j.bpj.2022.02.029
© 2022 Biophysical Society.

for the repositioning as was shown by knockout experiments (34–38). The dynein colocalizes with the adapter protein ADAP that forms a ring at the IS periphery after activation of the T cell (39,40). Dynein plays a key role in the two mechanisms proposed to drive the repositioning: cortical sliding and capture shrinkage. In the cortical-sliding mechanism the dyneins step to the minus-end of MTs (toward the MTOC) while being anchored on the cell membrane and therefore pull the MTOC toward the IS (15,39,41). It was indicated that the ring-shaped pSMAC is the place where attached dyneins are anchored (15,39). It was shown in (42) that the recruitment of the dynein to the IS is correlated and promoted by the depletion of cortical actin filaments from the same place.

A detailed analysis of the capture-shrinkage process was performed by Yi et al. (12). An optical trap was used to place the target cell so that the IS (contact zone) is initially diametrically opposed to the MTOC. This well-defined initial configuration allowed quantitative dynamical imagining including observation of the MT cytoskeleton morphology. They provided strong evidence that the repositioning is driven by a capture-shrinkage mechanism (43) involving the depolymerization of the caught MT in a confined area in the center of the IS. It was shown (12) that MTs bend alongside the cell membrane to reach the IS. Consequently, the MTs caught by their plus-end in the center of the IS straighten, form a narrow stalk, and depolymerize at the capture-point. The MTOC is pulled to the center of the IS, which invaginates the cell, indicating the location of the main pulling force. The capture-shrinkage mechanism was identified as the main driving force of the repositioning, since inhibiting the MT depolymerization substantially slowed down the repositioning. Yi et al. (12) reported that the repositioning can be divided into two phases that differ in the MTOC speed and the direction of its motion. In the first so-called polarization phase, the MTOC travels quickly in a circular motion around the nucleus. In the second, docking phase, the MTOC moves slowly and directly toward the IS.

T cells can attack two target cells simultaneously, in which case two IS are established (15). In this case, the MTOC transits repeatedly between the two IS (15), reminiscent of mitotic spindle oscillations in *Caenorhabditis elegans* (35,44–49). These spontaneous spindle oscillations have been explained by the cooperative attachment and detachment of cortical force generators to astral microtubules (50–53). For MTOC oscillations in T cells with two synapses a similar scenario has been proposed in connection with cortical-sliding mechanism (54). There it has been hypothesized that MTs on the trailing side of the MTOC are lifted off the pulling surface by viscous drag in the cytoplasm, leading to their detachment from cortical motors. Here we propose a different mechanism, which also works for capture shrinkage as reported in (12) and which relies on dynamic MTs, similar to, for instance, meiotic nuclear oscillations in *Schizosaccharomyces pombe* (55–57).

The interplay between dyneins and filaments is influenced by dynamic MTs, which constantly grow and shrink: periods of grow alternate with periods of rapid depolymerization in a process called dynamic instability (DI) (58–68). This process allows the cytoskeleton to adopt itself to the needs and functions of the cell to perform substantial shape changes through the cell cycle (61,69–71). Transitions between two IS would not be possible without the DI of MTs: at the end of the repositioning process toward one IS, the MT cytoskeleton is deformed and capture-shrinkage MTs are depolymerized (12,72). Due to DI, the depolymerized MTs regrow and the deformed cytoskeleton can restructure.

The main reason for MTOC oscillations in T cells with two IS as well as mitotic spindle oscillations to occur is that one has two distinct locations of dynein accumulation on the cell boundary, where motors can catch the MTs. The attachment of dynein is stochastic and one location wins the tug-of-war between the attached dyneins, resulting in MTOC relocation toward that location. In both cases, dyneins detach as the MTOC approaches. In the case of spindle oscillation, two restoring forces pushing the spindle back to the center were considered: the cortical pushing of the MT polymerization-driven growth against a barrier followed by the bending of the filaments, and the pulling force of the dyneins opposite to the movement of the MTOC (44–46,73–77). The purpose of our theoretical study is to elucidate the potential mechanisms for cooperative dynein attachment and detachment leading to stable, bistable, or oscillatory MTOC relocation in T cells with two IS.

COMPUTATIONAL MODEL

We use the computational model introduced in (72). The cell membrane and the nucleus are represented by two spheres with radius 5 μm and 3.8 μm, respectively. MTs sprout from the MTOC to the cell periphery, as sketched in Fig. 1, *a* and *b*. They are modeled by a bead-rod model with constrained Langevin dynamics. The MTs move under the influence of several forces—bending, drag, molecular motors, noise, and repulsive forces—keeping them between the nucleus and the cell membrane. The MTOC moves to the IS due to the pulling force of dyneins acting via two mechanisms: cortical sliding during which the plus-end of the MT remains free and the filament slides tangentially along the plasma membrane; and capture shrinkage, by which dyneins capture the tip of the MT and depolymerize it by pulling it against the membrane, as sketched in Fig. 1 *c*. Dyneins acting via cortical sliding and capture shrinkage are located in the complete IS and the narrow center, respectively. The two regions are represented by intersections of the cell sphere with cylinders with radius $R_{\mathrm{IS}} = 2$ μm for the complete IS and $R_{\mathrm{CIS}} = 0.4$ μm for the center, as sketched in Fig. 1. Note that we assume the dyneins to be immobile and firmly fixed at the cell boundary. This is in contrast to a recently proposed model in which

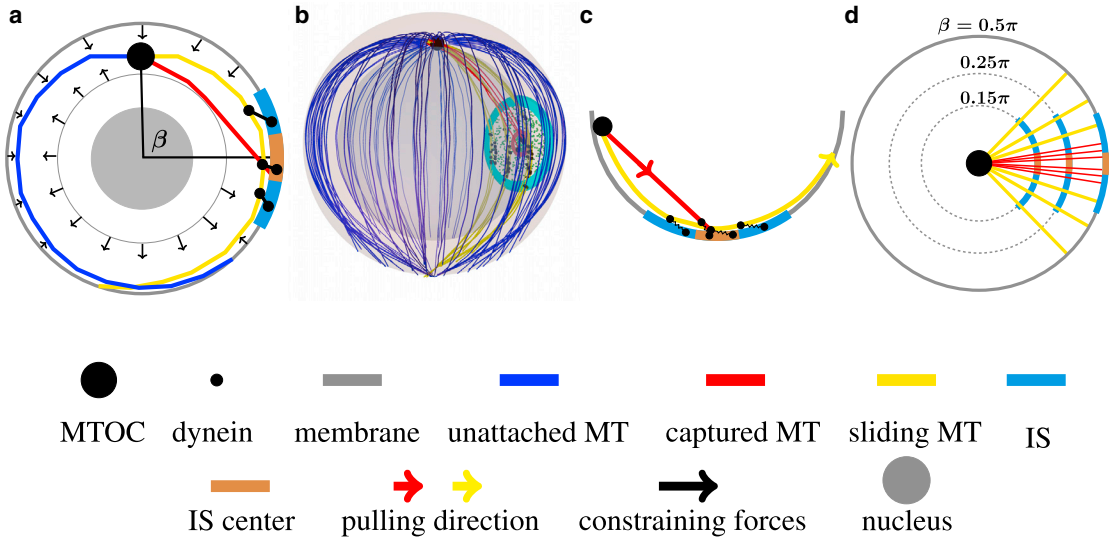

FIGURE 1 Sketch of the model of the cell with one IS. (*a*) A two-dimensional cross-section of the model is shown. The movement of the MTs sprouting from the MTOC is confined between the nucleus and the cell membrane. MTs are pulled by the cortical-sliding and capture-shrinkage mechanisms employing dynein motors in the IS and its center, respectively. Small black dots on the membrane and on the MTs represent dynein's anchor and attachment points, respectively. Angle β denotes the angle between the IS and the initial position of the MTOC. (*b*) Three-dimensional sketch. The plasma membrane and the nucleus are represented by the transparent outer and inner spheres, respectively. Small green spheres represent unattached dyneins in the IS and its center encircled by the cyan and brown rings, respectively. (*c*) Sketch of the cortical-sliding mechanism and the capture-shrinkage mechanism. Small black dots represent dynein's anchor and attachment points. When an MT is pulled by the capture-shrinkage mechanism, the plus-end of the MT is anchored at the center of the IS and depolymerizes. Cortical-sliding MTs slide on the surface and the MT plus-end remains free. (*d*) Sketch of MTs intersecting the IS and its center in the cells with different angles β. The percentage of MTs intersecting the IS is given by the ratio of the diameter of the IS to the cell circumference corresponding to angle β depicted by dashed circles. It is minimal at $\beta = 0.5\pi$. To see this figure in color, go online.

dyneins can more or less freely (dependent upon assumed friction coefficients) move in an actin-depleted zone of the IS (78) and thus self-organize into clusters at the boundary of the actin-depleted zone. This is an interesting hypothesis that has still to be confirmed or refuted by experiments, but we do not expect dyneins that can move within a restricted region of the IS to alter our main conclusions substantially, for which reason we stick to our original model of a predefined dynein location (72). In (72) we focused on the analysis of the MTOC repositioning process in the experimental setup used in (12), in which the MTOC and the IS are initially diametrically opposed. Here we consider naturally occurring situations, in which the angle β between the MTOC and the IS (see Fig. 1 *a*) is arbitrary, and situations in which the T cell attaches simultaneously to two target cells and thus forms two IS (15).

To analyze the situation with two IS, we augmented our model presented in (72) in several ways. The configuration of a cell with two IS is defined by the angle γ between the lines connecting the centers of IS with the center of the cell, sketched in Fig. 2 *a*. Both IS and the center of the cell are located on the *xz* plane of the coordinate system, sketched in Fig. 2 *b* and visually demonstrated in Fig. 2 *c*. The dyneins from both IS are in a tug-of-war leading to an increase of the detachment rate (72). When all capture-shrinkage dyneins detach from the MT, the plus-end is no longer fixed on the cell membrane. Most importantly, we included the dynamical instability of MTs (59,61,62,65,79), since we hypothesized that transitions between two IS rely on DI. The measured values of parameters of DI differ (59,80–89); they depend on the cell phase (90,91) and on the distance from the cell membrane (92–95). We take the following estimates from the literature: growth velocity $v_g = 0.1\ \mu\text{m s}^{-1}$ (62,83,89,96), although it might depend mildly on load and MT plus-end location (67,93); shrinking velocity $v_s = 0.2\ \mu\text{m s}^{-1}$; rescue rate (the transition rate from shrinkage to growth) $r_r = 0.044\ \text{s}^{-1}$ (80,82,97,98); and a length-dependent catastrophe rate (transition rate from growth to shrinkage) $c_r(L) = \exp((L - L_c)/b_c)\ \text{s}^{-1}$, where $L_c = \pi R_{\text{Cell}} + \frac{R_{\text{Cell}}}{2}$, $b_c = (L_0 - L_c)/\ln(r_c)$, $L_0 = \pi R_{\text{Cell}}$, and $r_c = 0.022$, reflecting a lower catastrophe rate close to the MTOC and a higher one at the cell periphery (69,92,99). The MT length distribution resulting from the DI with aforementioned parameters is shown in Fig. 2 *f*. Due to the DI, growing and shrinking MTs coexist in a dynamically changing cytoskeleton affected by the two mechanisms in both IS, as visualized in Fig. 2 *c*. The DI adds another force acting on MTs, since the growing tips of filaments are pushed against the cell membrane, sketched in Fig. 2 *e*. In contrast to the dynein forces, growing tips can push the MTOC from both IS and the *xz* plane. Since the plus-end of the MTs remains free during the cortical-sliding mechanism, the MTs can grow or shrink even when attached. The MT length influences the contact between MTs and the dyneins on the cell membrane. The MTOC is

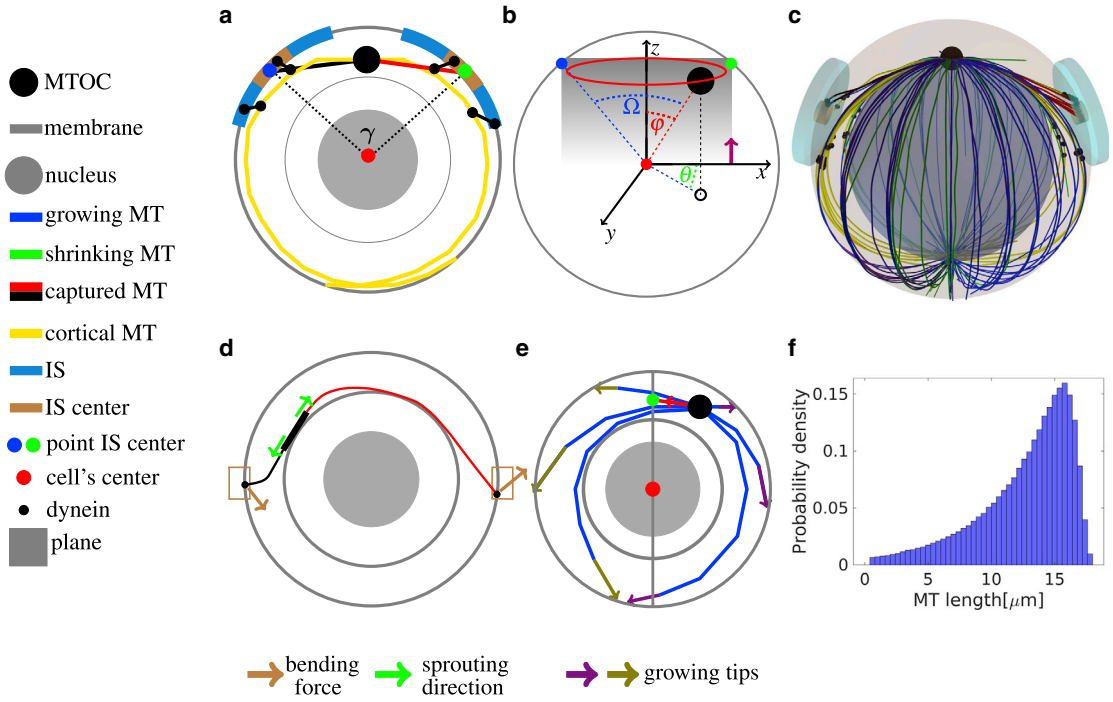

FIGURE 2 Sketch of the model of the cell with two IS. (*a*) γ denotes the angle between the two IS. Small black dots on the membrane and MTs represent dynein anchor and attachment points, respectively. MTs can attach to capture-shrinkage or cortical-sliding dyneins in both IS. (*b*) Sketch of the azimuthal (θ), polar (φ) and MTOC-IS (Ω) angle. The positions of the centers of both IS and the cell are located in the gray-shaded *xz* plane. When $\gamma<\pi$ both IS are located in the upper hemisphere ($z>0$) denoted by the magenta arrow. The polar angle φ denotes the cone with the vertex located in the center of the cell indicated by the red circle and the red dashed line. The azimuthal angle θ denotes the angle between the *x* axis and the dashed black line connecting the center of the cell with the projection of the MTOC position on the *xy* plane depicted by the small black circle. The angle Ω denotes the angle between the line connecting the MTOC with the cell center (red dashed line) and the axis of the IS depicted by the blue dashed line. (*c*) Three-dimensional snapshot of an initial configuration of the model with $\gamma = \frac{3}{4}\pi$. The point of view is located on the *yz* plane in the upper hemisphere ($z>0$) at the angle $\frac{\pi}{4}$ of the *y* axis. Growing and shrinking MTs radiate from the MTOC toward the cell periphery and can be pulled by the two mechanisms in both IS. Dyneins in one IS cooperate and dyneins from different IS are in a tug-of-war. (*d*) Sketch of bending forces acting on MTs attached to a capture-shrinkage. The thick black segment and the brown rectangles represent the plane of the MTOC and the centers of IS, respectively. The small black circles represent dyneins at points where they capture the plus-end of MTs. Since attached MTs sprout from the MTOC, bending forces push the long MT against the cell membrane and pull the short MT from it. (*e*) Two-dimensional sketch of the forces pulling the MTOC toward and away from the IS. The gray line represents the *xz* plane on which the centers of the cell and both IS are located. The red line stands for the MT attached in the IS. Dynein forces acting on the red MT pull the MTOC to the *xz* plane where the IS is located. The growing olive and violet plus-end of MTs push the MTOC from the *xz* plane and toward it, respectively. (*f*) Probability density of MT length. To see this figure in color, go online.

modeled as a planar structure (72), and the MT sprouts from the MTOC radially. The short MTs have to bend to stay in contact with the dyneins on the membrane, as sketched in Fig. 2 *d*. Once the dyneins detach, the tip recedes from the membrane, making the reattachment unlikely. On the other hand, bending forces press the tip of a long MT against the cell membrane where it can attach to dyneins.

We analyzed the role of the cortical-sliding and capture-shrinkage mechanisms during the MTOC repositioning in the cell with one and two IS by computer simulations of the model as defined in (72) and above. We mainly focused on the dependence of the repositioning process from initial conditions (angle β in Fig. 1 *a* for one IS) or double-IS arrangement (angle γ in Fig. 2 *a* for two IS), and from the cortical-sliding dynein density $\tilde{\rho}_{\mathrm{IS}}$ and capture-shrinkage dynein density ρ_{IS}. Since both densities are unknown, we varied them over the whole range from 10 to 1000 $\mu\mathrm{m}^{-2}$: lower densities fail to relocate the MTOC at all, and larger densities are not realistic due to steric repulsion between the dyneins. The angles β and γ were varied between 0.2π and π; smaller values appear unrealistic for geometric reasons (IS and MTOC size) while larger values can be mapped on the considered interval.

We implemented the model in C++ on a computer cluster with Intel(R) Xeon(R) CPU E5-2660 0 @ 2.20GH processors, Linux operating system (Arch-Linux 4.1.7-hardened-r1), and compiler g++ 4.9.2 and performed simulation runs to generate the data shown in this publication. The program listing is publicly available on GitHub (100). The snapshots from the simulations and videos in supporting material were made in POV-Ray.

RESULTS

Repositioning time scales

Before we present the results of computer simulations of the model defined in the previous section, we give an estimate

for the time scale of the MTOC repositioning process based on the antagonistic interplay of friction and pulling forces acting on the MT cytoskeleton and compare it with the repositioning times from experiments.

The MTOC position during the repositioning was traced in several experiments (14,15,101). The MTOC was originally located approximately at the opposite side of the target cell, and its repositioning to the IS took more than 3 min. The repositioning was faster in the experiments performed by Yi et al. (12) where the MTOC gets to the IS (distance < 2 μm) on average in ca. 2 min. The increased speed is likely caused by the experimental setup in which the MTOC and the target cell are initially diametrically opposed. In such a configuration all MTs that are long enough intersect the center of the IS, visually demonstrated in Fig. S2, *b* and *g*, and their plus-ends attach and are pulled by capture-shrinkage dyneins. Moreover, all MTs long enough to reach the IS can attach to cortical-sliding dyneins. When $\beta<\pi$, fewer dyneins are attached to MTs, since just a fraction of MTs intersect the IS and its center, see Fig. S1 *c* and visually in Fig. S2. Consequently, the initial diametrical opposition of the MTOC and the IS may result in higher pulling forces.

In what follows, we estimate the time scales as one would predict them on the basis of our model assumptions. The drag force acting on an MT moving with velocity v is $F_{\text{drag}} = \gamma_{\text{MT}} \times v$, where γ_{MT} is the drag coefficient. For a cylindrical object of length L and diameter d it is given by (102)

$$\gamma_{\text{MT}} = \frac{4\pi\mu L}{\ln(L/d) + 0.84}, \tag{1}$$

where μ is the viscosity of the surrounding liquid, the cytoplasm, which is e times the viscosity of water, $\mu = e \times \mu_w \approx 10^{-3}\text{N s m}^{-2} = e \times 10^{-3}\text{N s m}^{-2}$, and we estimate it to be $e \approx 30$ (72). Note that for simplicity we do not discriminate between movement of the cylindrical object in the longitudinal or in the transverse direction. Taking the average length of the MT to be $L = 10$ μm and its diameter to be $d = 25$ nm, we have $\gamma_{\text{MT}} \approx \mu \times 18.4$ μm. The drag coefficient of the whole cytoskeleton with N_{MT} MTs is $\gamma_{\text{cyto}} = N_{\text{MT}} \times \gamma_{\text{MT}}$. Mitochondria, Golgi apparatus (103–106), and endoplasmic reticulum (107–111) are massive organelles entangled with the cytoskeleton (14,19) and dragged with it, thereby increasing the drag coefficient by a factor g, i.e., $\gamma_{\text{eff}} = g \times \gamma_{\text{cyto}}$, which was estimated to be $g \approx 3$ (72).

The force pulling on the cytoskeleton is given by the number of dyneins attached to MTs times the average forces exerted by a dynein motor: $F = N_{\text{dyn}} \times F_{\text{dyn}}$, the latter is in the pico-Newton range, $F_{\text{dyn}} = f \times 10^{-12}\text{N}$, with $f \approx 1$. Consequently, the velocity of the whole cytoskeleton movement when N_{dyn} are pulling is

$$v = \frac{F_{\text{dyn}}}{\gamma_{\text{eff}}} \approx 54 \times \frac{N_{\text{dyn}}}{N_{\text{MT}}} \times \frac{f}{e\,g} \frac{\mu\text{m}}{\text{s}}. \tag{2}$$

Inserting the estimates $f = 1$, $e = 30$, $g = 3$, and evaluating the r.h.s. for $N_{\text{MT}} = 100$ MTs and $N_{\text{dyn}} = 10 - 50$ attached dyneins, one obtains a velocity $v = 3.6 - 18$ μm min^{-2}, a range that agrees well with the experimentally determined MTOC velocities (12). For an initial MTOC position diametrically opposed to the IS the MTOC would have to travel a distance $D = \pi R_{\text{Cell}}$, where R_{Cell} is the radius of the cell, and with $R_{\text{Cell}} \approx 5$ μm and the above velocity estimate the whole relocation process would need 1–4 min, which also agrees with the experimentally reported relocation times (12).

Since the number of attached dyneins is the central quantity determining the speed of the relocation process, let us relate to the dynein density and the attachment rates that we use in our model. For the capture-shrinkage mechanism we assume dynein to be concentrated in a central region of the IS with radius $R_{\text{CIS}} = 0.4$ μm (i.e., an area of 0.5 μm^2) and with a dynein density ρ_{IS}. At medium density of $\rho_{\text{IS}} = 100$ μm^{-2} we have 50 dyneins located in this area and, since most MTs in our model reach this area, they could in principle all be attached: the average distance between dyneins is $D_{\text{d2}} = \rho_{\text{IS}}^{-1/2} = 100$ nm for the assumed dynein density and with the attachment rate decreasing exponentially with the distance (see Eq. 4 in supporting material) one has $p_{\text{a}} \approx 2$ s^{-1}, implying that attachment is fast in comparison with the duration of the relocation process. Actually, in our simulations we observe that initially ca. one-quarter of all MTs get attached to dynein, some of them even attached simultaneously to two dyneins. Consequently for $\rho_{\text{IS}} = 100$ μm^{-2} we have indeed initially 25–50 dyneins attached to MTs, resulting in an initial MTOC velocity of $v_{\text{MTOC}} = 9 - 18$ μm min^{-2}. In the later stage of the relocation process competing forces will slow down the MTOC velocity, which will be revealed by the actual simulations reported below.

These rough estimates hold for our model framework as well and can be elaborated more on the basis of more detailed model assumptions. Force exerted by attached dynein is assumed to depend on the length of the stalk between the attachment and the anchor point l_{d} and is expressed as $F_{\text{d}} = 0$ if $l_{\text{d}}<L_0$ and $F_{\text{d}} = k_{\text{d}}(l_{\text{d}} - L_0)$ otherwise, where $L_0 = 18$ nm is the length of the relaxed stalk and $k_{\text{d}} = 400$ pN μm^{-1} is the elastic modulus of the stalk, see Fig. S1 *a*. In our model, the dynein makes steps with the length $d_{\text{step}} = 8$ nm toward the minus-end of the MT. The stepping is very fast at zero load (the first two steps) and slows down as the force increases (72), and the movement stops at the stall force $F_{\text{S}} = 4$ pN. Since the MT depolymerizes and moves, the distance between the attachment and the anchor point can differ from the multiples of the dynein step. Consequently, the length of the stalk is $l_1<l_{\text{d}}<l_2$ where l_1 and l_2 are the lengths corresponding to the second step and to the stall force, respectively, see Fig. S1 *a*. The average dynein force $\overline{F}_{\text{d}} = 1.66$ pN is calculated as the integral of the force between l_1 and l_2 divided by their distance.

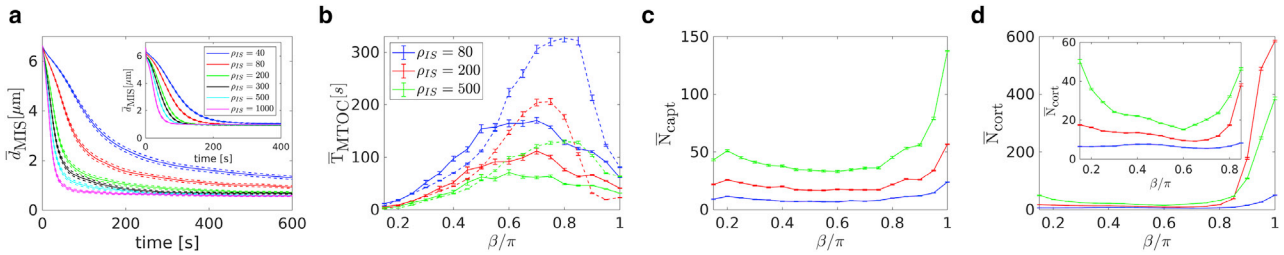

FIGURE 3 Repositioning under the influence of the capture-shrinkage and cortical-sliding mechanisms for different angles β between the IS and the initial position of the MTOC. (*a*) Dependence of the average MTOC-IS distance $\overline{d}_{\mathrm{MIS}}$ on time. $\beta = 0.5\pi$. The error bars are represented by dashed lines.(*b*) Dependence of the averaged times $\overline{T}_{\mathrm{MTOC}}$ (MTOC-IS distance d_{MIS}<1.5 μm) on the angle β. Capture-shrinkage and cortical-sliding mechanisms are represented by solid and dashed lines, respectively. (*c* and *d*) Dependencies of the mean numbers of attached dyneins $\overline{N}$ averaged over simulation runs on the angle β. (*c*) Capture-shrinkage mechanism. (*d*) Cortical-sliding mechanism. Dependencies are plotted with error bars. To see this figure in color, go online.

At the beginning of the repositioning the number of attached dyneins increases rapidly, see Fig. S3. The detachment rate of the dynein increases exponentially with the dynein force (Eq. S3). The detachment rate corresponding to the average dynein force is $p_{\mathrm{det}}(\overline{F}_{\mathrm{d}}) = 2.29\ \mathrm{s}^{-1}$, see Fig. S1 *b*. Consequently, dyneins are expected to detach in less than half a second. The attachment rate of the dynein decreases exponentially with the distance from the filament (72). When the distance between the dynein and the filament $d_{\mathrm{md}} = 95$ nm, the attachment rate equals detachment rate of the average dynein force $p_a(d_{\mathrm{md}}) = p_{\mathrm{det}}(\overline{F}_{\mathrm{d}})$, see Fig. S1 *b*. Consequently, the dyneins located closer to the filament are expected to attach faster than dyneins detach on average. The fraction of MTs intersecting the IS, q_{IS} (or the central region of the IS, q_{CIS}), shown in Fig. S1 *c*, is given by the ratio of the diameter of the IS (or diameter of the center of the IS) and the circumference $c(\beta)$ of the circle of latitude at angle β (see Fig. 1 *d*): $q_{\mathrm{IS}} = \min(1, 2R_{\mathrm{IS}}/c(\beta))$, with $c(\beta) = 2\pi r(\beta)$, where $r(\beta) = R_{\mathrm{Cell}}\sin(\beta)$ is the radius of the circle.

The number of attached dyneins can then be estimated by the number of dyneins that are closer than $d_{\mathrm{md}} = 95$ nm to an MT:

$$\overline{N}_{\mathrm{dm}} = N_{\mathrm{MT}} \times q_{\mathrm{CIS}} \times n_{\mathrm{dm}}, \tag{3}$$

where $N_{\mathrm{MT}} = 100$ is the number of MTs and $n_{\mathrm{dm}} = \pi \times d_{\mathrm{md}}^2 \times \rho_{\mathrm{IS}}$ is the number of dyneins in the proximity of the filament. It can be seen in Fig. S3 that the number of attached dyneins approaches the estimated number of dyneins regardless of the angle and the dynein density. With this β-dependent estimate of the β-dependent number of attached dyneins, we can perform again the calculation of the estimated MTOC velocity and the relocation time as above.

Fig. S1 *d* shows the dependence of the estimated time of the repositioning T_{est} on the angle β. The repositioning time increases with the angle until they reach a maximum at $\beta \sim 0.6\pi$ and then they decrease, see Fig. S1 *d*. The decrease when $\beta \leq 0.5\pi$ can be explained by the fact that the distance is increasing and the q_{CIS} decreases with β, see Fig. S1 *d*. The ratio q_{CIS} increases sharply when $\beta > 0.65\pi$ and the increased pulling force results in faster repositioning. This may offer an explanation as to why the time of repositioning is the shortest in the experimental setup when the MTOC and the IS are initially diametrically opposed (12).

Repositioning with one IS

In the first part of our work (72), we analyzed the repositioning in the cell where the MTOC and the IS are initially diametrically opposed. In this section we present the results of the computer simulation of the model with one IS, located at an angle β with respect to the initial position of the MTOC, see Fig. 1. Fig. 3 *a* shows that as expected the repositioning becomes faster with increasing dynein density for both mechanisms. Moreover, we found that the time scale for the completion of the relocation process agrees for a wide range of dynein densities. In addition, the MTOC dynamic has the same characteristic as in the case of $\beta = \pi$, which was analyzed in detail in (72). The MTOC travels to the IS and its speed decreases with the MTOC-IS distance. Additional analysis of the repositioning for the cases of $\beta = 0.75,\ 0.5,\ 0.25\pi$ can be found in sections 3.1 and 3.2 of supporting material. Here we focus on the average repositioning time $\overline{T}_{\mathrm{MTOC}}$ and its dependence on the angle β: Fig. 3 *b* shows that $\overline{T}_{\mathrm{MTOC}}$ increases with the angle β to a maximum at $\beta \sim 0.75\pi$ and then decreases. $\overline{T}_{\mathrm{MTOC}}$ depends on the initial MTOC-IS distance, opposing forces and the pulling force of dynein motors. The opposing forces increase with the angle β since the nucleus increasingly presents an obstacle on the path of the MTOC. For $\beta = 0.25\pi$ the nucleus does not intersect the line between the initial positions of the MTOC and the IS, visually demonstrated in supporting material and Fig. S2, *b–k*. Contrarily, the MTOC has to navigate around the entire nucleus when $\beta = \pi$.

Fig. 3, *c* and *d* show that the number of attached dyneins decreases with β to a minimum at approximately $\beta = 0.6\pi$ and then increases sharply. This can easily be explained by the number of MTs intersecting the IS given by the ratio of the diameter of the IS (or its center) and the circumference

of the circle of latitude at angle β (see Figs. 1 *d* and S1 *c*): $q_{IS} = \min(1, 2R_{IS}/c(\beta))$, with $c(\beta) = 2\pi r(\beta)$, where $r(\beta) = R_{Cell}\sin(\beta)$ is the radius of the circle. In the special case of $\beta = \pi$ all MTs long enough intersect the IS, as visualized in Fig. S2, *c* and *h*. However, when $\beta = 0.5\pi$ the IS is intersected only by MTs sprouting from the MTOC toward it, visually in Figs. 1, *b* and *d* and 2, *a* and *e*. The ratio decreases with the angle β until it reaches the minimum at $\beta = 0.5\pi$ and then it increases sharply, see Fig. S1 *c*, visually demonstrated in Fig. 1 *d*. In the simulations the minimum is slightly shifted from $\beta = \pi/2$ to 0.6π, as visible in Fig. 3, *c* and *d*, because dyneins detach due to an increasing opposing force of the nucleus. Subsequently, the number of dynein increases due to the fact that the increasing percentage of MTs intersects the IS, compare Fig. 3, *c* and *d* with Fig. S1 *c*. By comparing Fig. 3, *c* and *d* one observes that the number of attached cortical-sliding dyneins increases more sharply with increasing β, due to the fact that a part of the relatively large IS is located in the diametrical opposition of the IS for $\beta > 0.9\pi$ and the MTs sprouting from the MTOC in all directions can attach to dynein. The number of attached capture-shrinkage dyneins at $\beta = 0.15\pi$ is smaller than for $\beta = 0.2\pi$ due to the fact that owing to the short MTOC-IS distances the MTOC is dragged toward the IS and the number of dyneins quickly decreases, see Fig. S5.

The repositioning time, $\overline{T}_{MTOC}$, increases with β between 0 and $\beta < 0.7\pi$, since the distance and opposing force increase and the number of attached dyneins decrease, see Fig. 3, *b–d*. It can be seen in Fig. 3 *b* that the increase of $\overline{T}_{MTOC}$ is sharper for cortical sliding when $\beta > 0.5\pi$ due to the different behavior of the number of attached dyneins, cf. Figs. S5 and S7. When $\beta > 0.8$, $\overline{T}_{MTOC}$ decreases rapidly due to the sharp increase of pulling force.

The repositioning time offers a way to compare the performance of the two mechanisms for different configurations of the cell. It can be seen that the cortical-sliding mechanism outperforms the capture-shrinkage mechanism when $\beta < 0.5\pi$ and is substantially slower otherwise. The only exception is the case of cortical-sliding mechanism when the density $\tilde{\rho}_{IS} = 200\ \mu m^{-2}$ since it results in the fastest repositioning when $\beta \geq 0.85\pi$. The speed of the process can be explained by the three regimes of cortical-sliding repositioning analyzed in (72). The difference between the repositioning times for the two mechanisms decreases as the dynein density increases, see Fig. 3 *b*.

In our model the cortical-sliding dynein was distributed equally over the entire IS. However, we observe that the large majority of attached cortical-sliding dyneins is located at the periphery of the IS, see Fig. S8. In the case of combined mechanisms, the attached cortical-sliding dyneins are completely absent in the center of the IS, see Fig. S10 *c*. It was hypothesized (15) that the dynein colocalizes with the ADAP ring at the periphery of the IS to facilitate the interaction with MTs. This finding supports the aforementioned hypothesis.

It was also shown in (72) that the mechanisms act in synergy regardless the initial configuration of the cell, see Fig. S10, *a* and *b*, since the dominant mechanism is always supported by the secondary one. The cortical-sliding mechanism supports the capture-shrinkage mechanism by passing MTs to it, see Fig. S10, *f* and *i*. The capture-shrinkage mechanism supports cortical sliding by providing a firm anchor point and pulling the MTOC from the nucleus, see Fig. S10, *g* and *h*. When the MTOC recedes from the nucleus, MTs copy the cell membrane more closely and the attachment to cortical sliding is more likely, see Fig. S10 *e*. The dyneins of the two mechanisms pull in alignment sharing the load from opposing forces, resulting in decreased detachment probability. The combination of two mechanisms with low area densities can be faster than the dominant mechanism with high densities (72), Fig. S10, *a* and *b*.

Repositioning in the T cell with two IS

In this section we present the results of the computer simulation of the model with two IS, as sketched in Fig. 2. The configuration of the cell is defined by the angle γ between the two IS, sketched in Fig. 2 *a*. The densities of dyneins anchored at both IS, $\tilde{\rho}^1_{IS}$ and $\tilde{\rho}^2_{IS}$, and the central region of the IS, ρ^1_{IS} and ρ^2_{IS}, are unknown model parameters, which we therefore vary over a broad range between 0 (no anchored dynein) and 1000 μm^{-2}. We calculate and analyze the following quantities: the transition frequency between the two IS, N_{tr} min^{-1}; the dwell times at one IS, which is defined as the time interval during which the MTOC-IS distance is smaller than 3 μm, T_d; and the longitudinal and transverse fluctuations of the MTOC by determining the time-averaged probability distribution of the polar, azimuthal, and MTOC-IS angles, φ, θ, and Ω, respectively, which are defined as sketched in Fig. 2 *b*. For each point in the parameter space, these quantities were averaged over 500 simulation runs. Each simulation run is initialized with all dyneins being detached. Results are shown with the standard deviation as error bars.

Capture-shrinkage mechanism

Video S1 shows the repositioning with two IS with the same density of capture-shrinkage dyneins $\rho^1_{IS} = \rho^2_{IS} = 400\ \mu m^{-2}$. In the first seconds of the simulation, MTs attach to dyneins at the left IS, visualized in Fig. 4 *a*, and the MTOC is dragged toward it. Captured MTs shorten and depolymerize, see Fig. 4 *b*. As the MTOC approaches the left IS, we observe that the number of attached MTs decreases as MTs detach and reattach in the center of the IS. Simultaneously, the plus-end of MTs intersect with the distant IS and are captured by dyneins, visually demonstrated in Fig. 4 *c*. Finally, all MTs are detached from the left IS at the end of the transition and the MTOC moves to the right IS. Due to the DI, MTs grow (blue lines) and

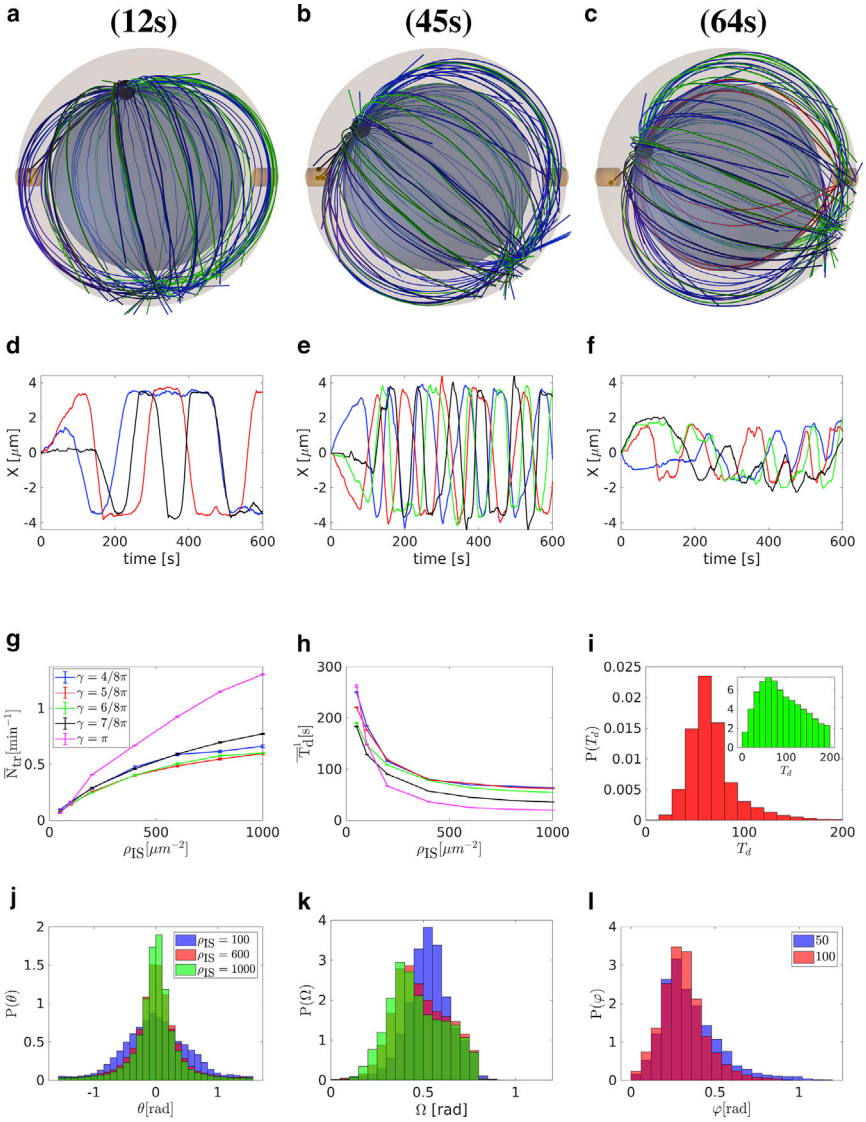

FIGURE 4 Capture-shrinkage mechanism with two IS with the same dynein density $\rho_{IS}^1 = \rho_{IS}^2 = \rho_{IS}$. (*a–c*) Snapshots from the time evolution of the MT cytoskeleton configuration with capture-shrinkage mechanism, $\rho_{IS} = 400\ \mu m^{-2}$. Symbols and colors as in Fig. 2. (*a*) MTs attach to dyneins in the left IS and form a stalk, and the MTOC moves toward the left IS. (*b*) MTOC approaches the IS and MTs depolymerize. (*c*) Short MTs detach from the left IS. Simultaneously, the plus-end of the MT intersects with the center of the distant IS and is captured by dynein. (*d–f*) Examples of the time evolution of the MTOC position in 600 s of the simulation. The time evolutions of x coordinate of the MTOC are shown. Both IS are located in the xz plane and the MTOC is originally located at the same distance from both IS, $x = 0$. (*d* and *e*) $\gamma = \pi$. (*d*) $\rho_{IS} = 200\ \mu m^{-2}$. (*e*) $\rho_{IS} = 800\ \mu m^{-2}$. (*f*) $\gamma = \frac{1}{2}\pi$, $\rho_{IS} = 800\ \mu m^{-2}$. (*g*) Dependencies of the average transition frequency between two IS per minute $\overline{N}_{tr}$. (*h*) Average dwell time that the MTOC spends next to the IS $\overline{T}_d^1$ (*h* on dynein density ρ_{IS}. Dependencies are plotted with error bars only if bigger than a symbol size. (*i*) Probability densities of dwell times for angle between the axis of two IS. $\gamma = \pi$, $\rho_{IS} = 200\ \mu m^{-2}$. Inset: dwell time distribution in a log-lin plot demonstrating the exponential tail. Dwell times were collected from 1280 simulation runs. (*j–l*) $\gamma = \frac{1}{2}\pi$. Probability densities of the azimuthal angle θ(*j*), MTOC-IS angle Ω (*k*), and polar angle φ (*l*). To see this figure in color, go online.

shrink (green lines). The MT cytoskeleton is not damaged permanently by the capture-shrinkage mechanism, since short filaments regrow due to the polymerization. Therefore, the MTOC relocates back and forth between the two IS until one IS is removed. In Fig. 4, *d–f* we see that the time evolution of the MTOC position follows a recurring pattern already seen in the video: the MTOC travels to one IS, remains in its close proximity for a time, and then repositions to the second IS. This pattern is caused by two effects: the MTs lose contact with the close IS (to which it moves) and establish a contact with the distant IS. The similar process for the case $\gamma = \frac{3\pi}{4}$ is shown in Video S2.

The physical mechanism underlying the MTOC transition from one IS to the other and back is the decrease of the dynein attachment probability with decreasing MTOC-IS distance due to strong bending of attached filaments at short distances, as sketched in Fig. 2 *d*. The MTOC is a planar structure and MTs sprout from the MTOC tangentially. At large MTOC-IS distances the MT bends around the nucleus and bending forces press the plus-end against the cell membrane, where it can be captured by dyneins. At small MTOC-IS distances an attached MT has to bend to stay in contact with the IS. When a short MT detaches from dyneins the plus-end recedes from the IS, making reattachment unlikely. The attachment probability of the MT in the IS depends on the circumferential MTOC-IS distance, since only MTs having a length roughly corresponding to it can attach in the IS. Fig. 2 *f* shows that the probability density of the MT length steadily increases before reaching a peak at $L_{MT} \sim 15.8\ \mu m$, corresponding to the circumferential distance between two IS when $\gamma = \pi$. Consequently, the probability of the MT attachment in the distant IS increases as the MTOC recedes, since an increasing number of MTs have a length corresponding to the circumferential MTOC-IS distance.

By comparing Fig. 4, *d* and *e*, one realizes that when the density increases, transitions are faster and the MTOC remains close to the IS for a shorter time. Fig. 4 *g* shows that the transition frequency increases with the dynein density. Dwell times decrease with the increasing dynein density and increasing angle γ, cf. Fig. 4 *h*. One would expect that the transition frequency decreases with the rising distance between two IS (increasing with γ). Surprisingly, it decreases with γ only when $\gamma \leq \frac{3\pi}{4}$ and is the maximal when $\gamma = \pi$.

The dynein detachment probability is force dependent and its pulling force is constantly opposed by forces of the friction and from the nucleus. As the density increases, more dyneins share the load from opposing forces and the detachment probability decreases, leading to shorter dwell times, cf. Fig. 4 *h*. Fig. 4 *i* shows the probability distribution of dwell times, and from the log-lin scale of the same plot in the inset one concludes that the dwell time distribution has an exponential tail. An increased dynein number leads to faster MTOC movement and shorter dwell times, which again result in an increased transition frequency.

The transition frequency does not decrease monotonously with increasing angle γ, since the probability of dynein attachment increases with the circumferential distance between two IS. At the end of the MTOC transition, only MTs having a length roughly corresponding to the circumferential distance between two IS can attach at the distant IS, as visualized in Fig. 4 *c*. The MT length distribution increases until it reaches maximum, corresponding approximately to the half of the cell circumference, cf. Fig. 2 *f*. Consequently, the probability that a plus-end intersects with the center of the IS at the end of MTOC transitions increases with the angle γ. The transition frequency decreases with the angle when $\gamma \leq \frac{3\pi}{4}$ because the MTOC travels longer distances and the increase of probability density is not significant. When $\gamma > \frac{3\pi}{4}$ the increasing distance is compensated by a higher number of MTs intersecting with the center of the distant IS, leading to shorter dwell times and faster MTOC movement, see Fig. 4, *e–h*. The case of $\gamma = \pi$ has the additional geometrical advantage that all MTs with sufficient length intersect the distant IS at the end of transitions, visually demonstrated in Fig. 4 *c*.

The increasing number of attached MTs influences the continuity of the MTOC transitions. When $\gamma = \pi$, the movement of the MTOC is regular and uninterrupted, see Fig. 4 *e*. On the other hand, for the smallest value of γ, i.e., the shortest distance between the two IS, the movement of the MTOC is highly irregular, see Fig. 4 *f*: the MTOC stops and stalls before resuming the movement to the IS (blue, green). In some cases the MTOC does not finish the journey and returns to the original location (black). When $\gamma = \pi$ a relatively high number of MTs intersects with the center of the distant IS with their plus-end, see Fig. 2 *f*. Since the MTOC is pulled by dyneins acting on multiple MTs, transitions are smooth and uninterrupted. When $\gamma = \pi/2$ only a limited number of MTs is pulled, resulting in easily interrupted transitions.

The longitudinal and transverse fluctuations of the MTOC along its path from one IS to the other can be described by the distribution of the polar and azimuthal angle, φ and θ, sketched in Fig. 2 *b*. The standard deviation of the azimuthal angle decreases with the increasing dynein density when $\gamma \leq \frac{3\pi}{4}$ and increases when $\gamma = \pi$, see Fig. S11 *a*. Two forces act on cytoskeleton: forces of dynein pulling the MTOC toward the IS and the forces of the tips of growing MTs on the cell membrane pushing the MTOC to all directions, sketched in Fig. 2 *e*. When $\gamma < \frac{3\pi}{4}$, only a small fraction of MTs sprouting from the MTOC intersect the distant IS at the end of the transition, see Fig. 2 *f*. Since the stalk pulls the MTOC either within the *xz* plane or toward it, sketched in Fig. 2 *e*, the azimuthal angle can only decrease during transitions. At the end of the transition, the dynein detach and forces from growing MT tips can push the MTOC from the *xz* plane, sketched in Fig. 2 *e*, increasing the azimuthal angle. Consequently, the standard deviation of the azimuthal angle decreases with dwell times and therefore decreases with dynein density, see Figs. 4 *h* and S11 *a*. Fig. 4 *j* shows that when $\gamma = \frac{\pi}{2}$ the peak of the probability distribution of the azimuthal angle is located at $\theta = 0$ and narrows for higher dynein densities, resulting in a reduced standard deviation. When $\gamma \geq \frac{7}{8}\pi$ the transitions can increase the azimuthal angle of the MTOC, since the MTs sprouting in multiple directions can attach to the IS, as visualized in Fig. 4. In contrast to the case $\gamma < \frac{7}{8}\pi$, the azimuthal angle increases as the dwell time decreases when $\gamma = \pi$, since the azimuthal angles are low when the MTOC is in the proximity of the IS and the transitions pulls it from the plane, increasing azimuthal angles of the MTOC, see Fig. S11, *a* and *c*.

When $\gamma < \pi$ the standard deviation of the polar angle slightly decreases with the dynein density when $\rho_{IS} < 100\ \mu m^2$ and then increases, see Fig. S11 *b*. The standard deviation of the polar angle depends on its range. When $\rho_{IS} \geq 100\ \mu m^2$ the MTOC transitions between two IS, see Figs. 4, *g* and *h*, and the rising dynein force pulls the MTOC closer to the IS, see Fig.4 *k*, increasing the range of the polar angle. The density of $\rho_{IS} = 50\ \mu m^2$ is an exceptional case since the MTOC does not transition, see Fig. 4 *g*, since the dynein density is too small to establish the MT stalk. Consequently, forces from the growing MTs can push the MTOC from both IS increasing the polar angle, see Fig. S4 *l*. Obviously, the standard deviation of the polar angle increases with γ, see Fig. S11. When $\gamma = \pi$, the standard deviation is the largest and increases monotonously with dynein density. When $\gamma < \pi$ dyneins always pull the MTOC to the IS located in upper hemisphere, sketched in Fig. 2 *b*. When $\gamma = \pi$ the MTOC can travel through the lower hemisphere, thus increasing the range of the polar angle. Consequently, the standard deviation of the polar angle increases with the transition frequency, compare

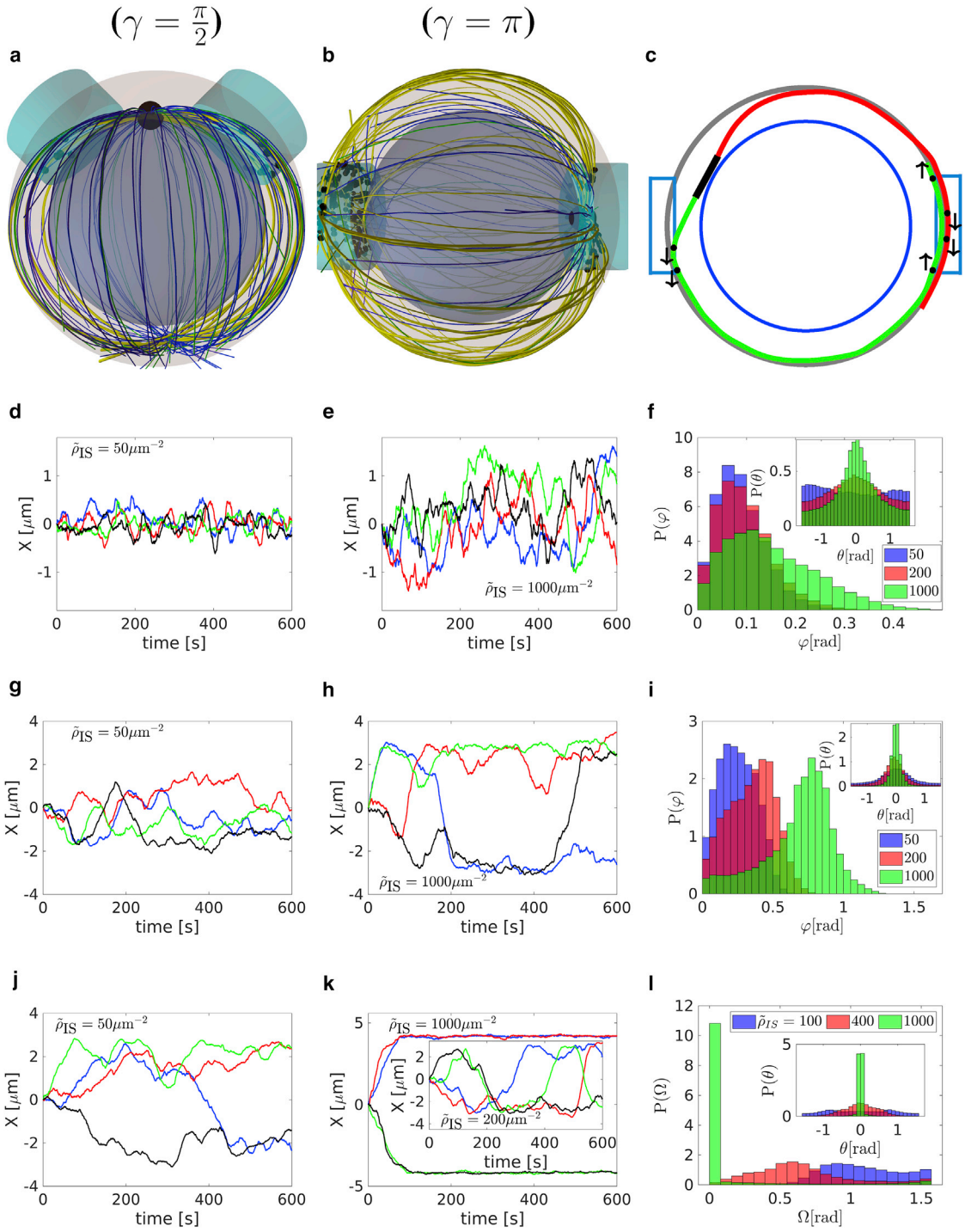

FIGURE 5 Cortical-sliding mechanism with two IS with the same dynein density $\tilde{\rho}_{IS}^1 = \tilde{\rho}_{IS}^2 = \tilde{\rho}_{IS}$. (*a* and *b*) Snapshots from the time evolution of the MT cytoskeleton configuration with the cortical-sliding mechanism acting at both IS. Symbols and colors as in Fig. 2. (*a*) $\gamma = 0.5\pi$, $\tilde{\rho}_{IS} = 200\ \mu m^{-2}$. MTs attach in both IS and dyneins remain in a tug-of-war for the rest of the simulation. (*b*) $\gamma = \pi$, $\tilde{\rho}_{IS} = 1000\ \mu m^{-2}$. The MTOC is located close to the center of the IS. Almost all MTs are attached to dyneins and they sprout from the MTOC in all directions. (*c*) Sketch of dynein forces when $\gamma = \pi$ and with the MTOC in the close proximity of the IS. The cell membrane and the nucleus are represented by the gray and blue circle, respectively. The black line and the cyan rectangles denote the MTOC and two IS, respectively. Black dots and arrows denote dynein motors and directions of pulling forces, respectively. The green MT is attached to dyneins in both IS and the red MT is attached only by dyneins in the distant IS. (*d* and *e*) Examples of the time evolution of the MTOC position for $\gamma = \pi/2$. The time evolutions of x coordinate of the MTOC are shown, (*d*) for $\tilde{\rho}_{IS} = 50\ \mu m^{-2}$, (*e*) for $\tilde{\rho}_{IS} = 1000\ \mu m^{-2}$. (*f*) Probability

(legend continued on next page)

Figs. S11 *b* and 4 *g*. Similarly to the case $\gamma<\beta$, the MTOC is pulled closer to the IS as the dynein density increases, see Fig. S11 *d*.

We further analyzed the capture-shrinkage scenario with different dynein densities at the two IS. As in the case of equal densities, dynein detaches when the MTOC approaches the IS and MTs attach at the second IS, visually in Fig. 4 *c*. We fixed the density in IS_1 $\rho_{IS}^1 = 600\ \mu m^{-2}$ and we vary the density in IS_2 $50\ \mu m^{-2} \leq \rho_{IS}^2 \leq 1000\ \mu m^{-2}$. From Fig. S12 *a* one can see that the MTOC transitions between two IS even when dynein densities are different. The MTOC is predominantly located closer to the IS with higher dynein density. Average MTOC-IS_1 angle $\overline{\Omega}$ steadily increases with ρ_{IS}^2 and $\overline{\Omega} = \frac{\gamma}{2}$ when $\rho_{IS}^2 = \rho_{IS}^1$, see Fig. S12 *b*. Moreover, the dwell times are substantially larger for the IS with higher density, see Fig. S12 *c*.

Cortical-sliding mechanism

In contrast to the capture-shrinkage mechanism, cortical-sliding dyneins are distributed in a relatively large IS and can attach at any position on an MT. Since multiple filaments intersect with the IS in every instant, MTs are always simultaneously attached at both IS, as visualized in Fig. 5, *a* and *b*.

By comparison of Fig. 5, *d–l* one realizes that as the angle γ increases, the MTOC transitions become more continuous and less frequent. When $\gamma<\frac{3\pi}{4}$, the transition frequency increases before reaching the peak at $\tilde{\rho}_{IS} = 200\ \mu m^{-2}$ and then declines, see Fig. S13 *a*. It steadily decreases with the rising dynein density when $\gamma>\frac{3\pi}{4}$. The case of $\gamma = \pi$ is unique since the transition frequency decreases to zero. Moreover, it is the only case when standard deviation of the polar angle decreases with rising dynein density, see Fig. S13 *b*. The standard deviations of the azimuthal angle steadily decrease with the dynein density, see Fig. S13 *c*.

When $\gamma<\frac{3\pi}{4}$ relatively large IS are located close to each other, visually demonstrated in Fig. 5 *a*. The dynein detach when the MTOC approaches the IS (see section 3.2 of supporting material) and the pulling force decreases. MTs are being pulled by dyneins in the second IS at the same time. These two effects result in minimal MTOC fluctuations around the central position, see Fig. 5 *d*, and in a relatively high transition frequency between two hemispheres, see Fig. S13 *a*. By comparison of azimuthal angles in Fig. 5, *f* and *i* one realizes that the MTOC fluctuations have a strong lateral component when $\gamma \leq \frac{3\pi}{4}$, which is stronger than the parallel one when $\tilde{\rho} = 50\ \mu m^{-2}$. This is due to the fact that dyneins located at the peripheries of both IS can cooperate while pulling the MTOC from the *xz* plane but are always in competition when pulling the MTOC parallel to the plane. The MTOC movement becomes more aligned with the *xz* plane, see Fig. 5 *f*, as the dynein density increases, leading to a slight increase in the transition frequency, see Fig. S13 *a*. As the density further increases, $\tilde{\rho}>200\ \mu m^{-2}$, the MTOC is increasingly pulled from the central position to the IS, see Fig. 5, *e* and *f*. The number of transitions decreases since the MTOC travels a longer distance. Moreover, as the MTOC approaches one IS the forces of nucleus oppose the movement to the distant IS, giving the advantage to the dynein at the close IS in the constant tug-of-war.

When $\frac{3\pi}{4} \leq \gamma<\pi$ and dynein densities are low, the constant competition between dyneins from both IS leads to short, interrupted transitions between two IS, see Fig. 5 *g*. The MTOC moves around the central position (green), and transitions between two IS are very slow (blue) or interrupted (red), or the MTOC dwells in one hemisphere for a long time (black). As in the previous case, the MTOC is increasingly pulled from the central position to the IS with rising density, see Fig. 5 *h* and *i*. Transitions to the distant IS become more unlikely due to the fact that the dyneins from the distant IS are opposed by the forces of dyneins from the close IS and from the nucleus. When $\tilde{\rho} = 1000\ \mu m^{-2}$ the MTOC dwells in one hemisphere and rarely transitions, see Fig. 5, *h* and *i*. Since the MTOC stays longer in the proximity of the IS located at the *xz* plane as the density increases, the peak of azimuthal angle probability distributions narrows, see Fig. 5 *i*. Video S3 shows the process for the case $\gamma = \frac{3}{4}\pi$ and $\tilde{\rho} = 600\ \mu m^{-2}$.

In Fig. 5, *j* and *k* it can be seen that the MTOC trajectories are fundamentally different for lower and higher densities when $\gamma = \pi$. Moreover, the transition frequency is higher than in the case of $\gamma = \frac{7\pi}{8}$, since the higher number of MTs intersect the distant IS when IS are in diametrical opposition, visually demonstrated in Fig. 5 *b*. When the density is low, the MTOC transitions between two IS, never reaching their center, see Fig. 5, *j* and *l*. As the density increases, the MTOC approaches closer to the IS, see Fig. 5, *k* and *l*. When $\tilde{\rho}_{IS}>600\ \mu m^{-2}$, dynein forces are strong enough to pull the MTOC to the center of the IS, where it remains for the rest of the simulation, see Fig. 5, *k* and *l*. In such a case the majority of MTs are attached in the distant IS, visually demonstrated in Fig. 5 *b*. Since MTs attached at the distant IS are sprouting from the MTOC in every direction, the dyneins act in a competition, sketched in Fig. 5 *c*. If the MTOC recedes from the center of the IS, the dyneins at the close IS pull the MTOC back alongside the part of the dyneins in the distant IS. Contrarily to the cases when $\beta<\pi$ the MTOC can travel to the distant IS in all directions, resulting in substantial deviations from the *xz* plane, see the inset of Fig. 5 *l*. The peak of the probability density of the

distribution of the polar angle φ (main plot) and the azimuthal angle θ (inset). (*g–i*) The same as (*d–f*) for $\gamma = \frac{2\pi}{3}$. (*j* and *k*) Examples of the time evolution of the MTOC position for $\gamma = \pi$, (*j*) for $\tilde{\rho}_{IS} = 50\ \mu m^{-2}$, (*k*) for $\tilde{\rho}_{IS} = 1000\ \mu m^{-2}$ (main plot) and $\tilde{\rho}_{IS} = 200\ \mu m^{-2}$ (inset). (*l*) Probability distribution of the MTOC-IS angle Ω and the azimuthal angle (inset). To see this figure in color, go online.

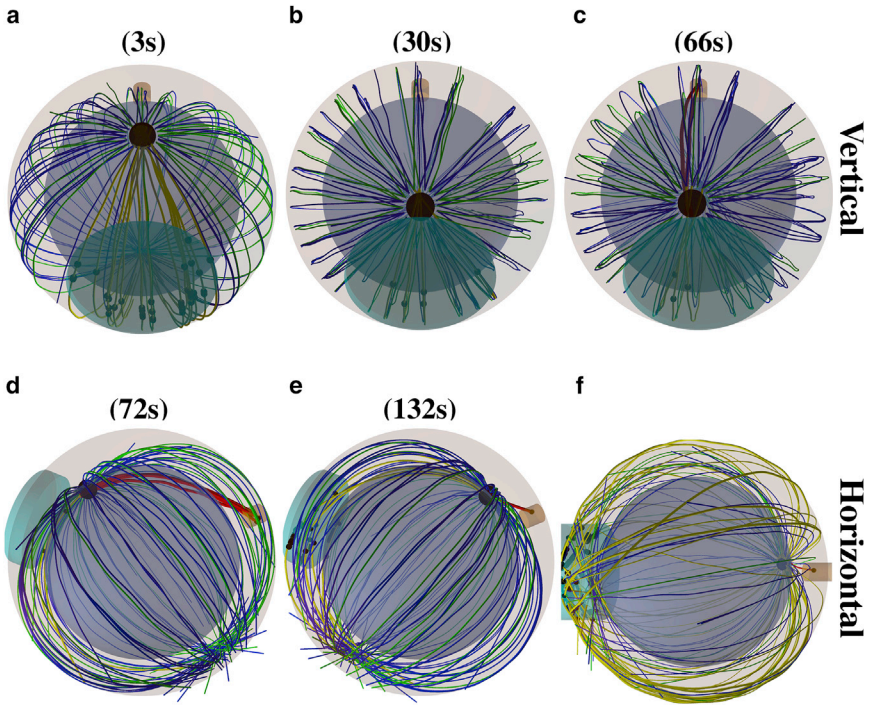

FIGURE 6 Snapshots from the time evolution of the MT cytoskeleton configuration under the effects of both capture-shrinkage and cortical-sliding mechanisms from two perspectives in different IS with the same dynein densities. $\gamma = \frac{3\pi}{4}$, $\rho^1_{IS} = \tilde{\rho}^2_{IS} = \rho = 400\ \mu m^{-2}$, $\rho^2_{IS} = \tilde{\rho}^1_{IS} = 0\ \mu m^{-2}$. Symbols and colors as in Fig. 2. (*a*) Initially, MTs attach only to the cortical-sliding dynein at the left IS since no plus-end of MTs intersect with the center of the right IS. (*b*) Cortical-sliding dyneins detach as the MTOC approaches the left IS. (*c*) The plus-end of an MT intersects with the center of the right IS and is captured by dynein. (*d*) Several MTs form a stalk connecting the center of the right IS with the MTOC and overpower cortical sliding at the left IS. (*e*) As the MTOC approaches the right IS, capture-shrinkage MTs detach from the dyneins. Simultaneously, MTs attach to cortical-sliding dyneins at the left IS. (*f*) Snapshots from the time evolution of the MT cytoskeleton. $\rho = 1000\ \mu m^{-2}$, $\gamma = \pi$. The MTOC is located close to the center of the right IS. Almost all MTs are attached to cortical-sliding dyneins at the left IS and they sprout from the MTOC in all directions, resulting in contradictory pulling forces. To see this figure in color, go online.

angle θ becomes more narrow with rising density, since the MTOC is increasingly located closer to the IS, see Fig. 5 *l*. Video S4 shows the process for the case $\gamma = \pi$ and $\tilde{\rho} = 1000\ \mu m^{-2}$.

In general, the MTOC is located closer to the *xz* plane as the density increases, see Fig. 5, *f*, *i*, and *l*. Consequently, the standard deviation of the horizontal angle decreases with the dynein density, see Fig. S13 *c*. At the same time the standard deviation of the polar angle increases, see Fig. S13 *b*, due to its increased range, see Fig. 5, *f* and *i*. The only exception is the case of $\gamma = \pi$. Small and still decreasing transition frequency causes decreasing range MTOC-IS_1 angles, see Figs. S13 *a* and 5 *l*, leading to the decreased standard deviation of the polar angle, see Fig. S13 *b*.

Capture-shrinkage and cortical-sliding mechanisms in different IS

In this section, we analyze the scenario when two IS employ different mechanisms. Cortical sliding has multiple advantages over the capture-shrinkage mechanism. Given the radii of the whole IS and its center $R_{IS} = 2\ \mu m^{-2}$ and $R_{CIS} = 0.4\ \mu m^{-2}$, respectively, the surface of the whole IS is 25-times larger than the surface of the IS center. Moreover, the cortical-sliding dyneins attach on the whole MT, with capture shrinkage just at the end. Consequently, multiple filaments are attached to cortical-sliding dyneins during the entire simulation. The capture-shrinkage dynein attach only when the tip of the MT intersects with the narrow center of the IS, making the attachment of capture-shrinkage dyneins far less frequent. All capture-shrinkage dyneins can be unattached for a long time. On the other hand, the capture-shrinkage mechanism has the advantage that the attached MTs form a narrow stalk assuring the alignment of dynein forces, as visualized in Fig. 6 *d*.

The resulting repositioning process is shown in Video S5, $\rho^1_{IS} = \tilde{\rho}^2_{IS} = 400\ \mu m^{-2}$. The capture-shrinkage dyneins are located in the right IS_1. The MTOC moves to the left IS, since the MTs attach immediately to cortical-sliding dyneins and the center of the right IS is not intersected by plus-ends of MTs, visualized in Fig. 6 *a*. When the MTOC approaches the left IS, the cortical-sliding dyneins detach and, simultaneously, the tips of MTs passing through the center of the right IS attach to capture-shrinkage dyneins, visually demonstrated in Fig. 6, *b* and *c*. Since the capture-shrinkage mechanism is opposed by cortical sliding, MTs can detach from the capture-shrinkage dyneins. It takes several MTs to attach in the center of the IS at the same time to compete with the force of cortical-sliding dyneins. As the force of capture-shrinkage dyneins outweighs the force of the cortical-sliding dyneins, the MTOC moves to the right center in the direction given by the MT stalk, visualized in Fig. 6 *d*. The capture-shrinkage dyneins detach when the MTOC approaches the right IS. Simultaneously, cortical-sliding dyneins attach at the left IS, visually demonstrated in Fig. 6 *e*, and the MTOC moves again to the left IS.

Fig. 7 *a* shows that when $\gamma < \pi$ the transition frequency steadily increases with the dynein density. Fig. 7 *b* shows that when the densities are low, the average angle between the MTOC and the capture-shrinkage IS_1 is $\overline{\Omega} \gg \frac{\gamma}{2}$, indicating

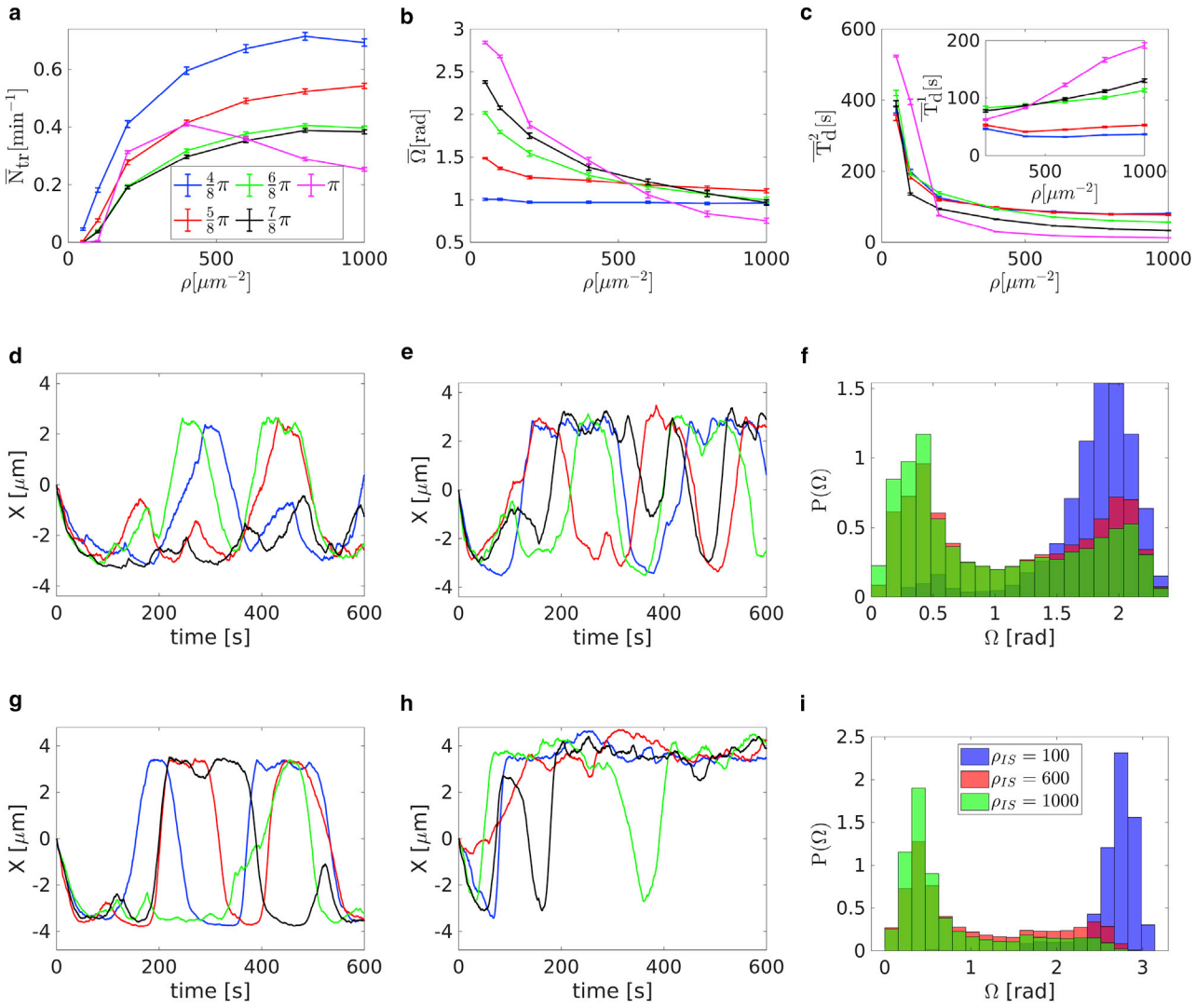

FIGURE 7 Capture-shrinkage and cortical-sliding mechanisms in different IS with the same dynein densities. $\rho^1_{IS} = \tilde{\rho}^2_{IS} = \rho$, $\rho^2_{IS} = \tilde{\rho}^1_{IS} = 0$ μm^{-2}. Cortical-sliding IS_2 is located in the hemisphere $x<0$. (*a–c*) Dependencies of the average transition frequency $\overline{N}_{tr}$ between two IS (*a*), the average angle between the MTOC and the capture-shrinkage IS_1 $\overline{\Omega}$ (*b*), and average dwell times $\overline{T}^1_d$ and $\overline{T}^2_d$ that the MTOC spends next to the capture-shrinkage IS_1 and the cortical-sliding IS_2, respectively (*c*), on the dynein density ρ. The dwell times $\overline{T}^1_d$ are given for $\rho \geq 200$ μm^{-2} since the MTOC does not reach the IS_1 when $\rho<200$ μm^{-2}. Dependencies are plotted with error bars only if bigger than a symbol size. (*d* and *e*) Examples of the time evolution of the MTOC position in 600 s of simulation. The time evolutions of x coordinate of the MTOC are shown, $\gamma = \frac{3\pi}{4}$. (*d*) $\rho = 200$ μm^{-2}, (*e*) $\rho = 1000$ μm^{-2}. (*f*) Probability distribution of the angle Ω between the MTOC and the capture-shrinkage IS_1, $\gamma = \frac{3\pi}{4}$. (*g* and *h*) Examples of the time evolution of the MTOC position in 600 s of simulation, $\gamma = \pi$. (*g*) $\rho = 200$ μm^{-2}, (*h*) $\rho = 1000$ μm^{-2}. (*i*) Probability distribution of the angle Ω between the MTOC and the capture-shrinkage IS_1, $\gamma = \pi$. To see this figure in color, go online.

that the MTOC is predominantly located closer to the cortical-sliding IS_2. Moreover, the angle decreases with the increasing dynein density. Average dwell times $\overline{T}^2_d$ close to cortical-sliding IS_2 and $\overline{T}^1_d$ close to capture-shrinkage IS_1 decrease and increase with increasing density, respectively, see Fig. 7 *c*.

It can be seen in Fig. 7, *d*, *e*, *g*, and *h* that initially the MTOC travels to the cortical-sliding IS_2 in all cases except one. The MTOC travels to the capture-shrinkage IS_1 only in a highly improbable scenario when plus-ends of multiple MTs intersect the narrow IS center. When $\gamma = \frac{3\pi}{4}$ and $\rho = 200$ μm^{-2} the MTOC dwells in the proximity of the cortical-sliding IS_2, see Fig. 7, *d* and *f*. The transitions to the capture-shrinkage IS_1 are interrupted and the MTOC travels back to the cortical-sliding IS_2 (black). When the MTOC finishes the transitions to the IS_1, it dwells in its proximity for a short time and then returns to the IS_2 (blue, red). Multiple transitions to IS_1 rarely occur (green). Interrupted transitions to IS_1 can be explained by constantly attached cortical-sliding dyneins overpowering the force of the

capture-shrinkage mechanism. If the MTOC finishes transition to the IS_1, capture-shrinkage dyneins detach and cortical sliding pulls the MTOC back to the IS_2. To conclude, cortical sliding has dominance over the capture-shrinkage mechanism when $\rho_{IS}<600\ \mu m^{-2}$, since the MTOC is located predominantly closer to the IS_2, see Fig. 7, *b–d* and *f*.

Fig. 7 *e* shows that when $\rho = 1000\ \mu m^{-2}$ the transitions toward the capture-shrinkage IS_1 are mostly uninterrupted, indicating that the capture-shrinkage mechanism can compete with cortical-sliding dyneins by capturing several MTs and forming MT stalk, as visualized in Fig. 6 *d*. Moreover, the MTOC dwells longer close to the capture-shrinkage IS_1, see Fig. 7, *c*, *e*, and *f*, resulting in the decrease of the average MTOC-IS_1 angle, see Fig. 7 *b*. Therefore, the capture-shrinkage mechanism gains dominance over the cortical-sliding mechanism as the dynein density increases.

When $\gamma<\pi$, the transition frequency increases with the dynein density, see Fig. 7 *a*, and therefore increases as the capture-shrinkage mechanism becomes dominant. The increasing density of capture-shrinkage dyneins increases the probability of dynein attachment and the formation of MT stalks that can overcome the cortical-sliding mechanism. The formation of the MT stalks results in complete transitions toward the capture-shrinkage IS_1 and in the steep decrease of cortical-sliding dwell times, see Fig. 7, *c* and *e*. However, the capture-shrinkage dwell times increase only slightly with the increasing density, see Fig. 7 *c*. Regardless of dynein density, motors detach at the end of the transition and depolymerized MTs are unlikely to reattach, visually demonstrated in Fig. 2 *d*. Consequently, as the dynein density increases, the capture-shrinkage mechanism becomes more able to pull the MTOC but remains unable to hold it, leading to the increased transition frequency.

The case of $\gamma = \pi$ is unique, since the transition frequency increases with the dynein density before reaching the peak at $\rho = 400\ \mu m^{-2}$ before slowly decreasing, see Fig. 7 *a*. The MTOC trajectories differ when considering multiple dynein densities. When $\rho = 200\ \mu m^{-2}$, the MTOC moves similarly to the case when $\gamma<\pi$. The MTOC transitions to one IS, dwells there, then moves to the second IS, see Fig. 7 *g*. Fig. 7 *i* shows that the MTOC is predominantly located closer to the cortical-sliding IS when the dynein density is low. When $\rho = 1000\ \mu m^{-2}$, the MTOC dwells in the proximity of the capture-shrinkage IS_1, see Fig. 7 *I*, and the transitions to the cortical-sliding IS_2 are infrequent and unfinished, see Fig. 7 *h*. When $\rho \geq 600\ \mu m^{-2}$, the dynein force is strong enough to pull the MTOC to the close proximity of the center of the capture-shrinkage IS_1, Fig 7 *i*. In such a case almost all MTs are attached to the cortical-sliding dynein at the distant IS_2, visually demonstrated in Fig 6 *f*. The MTOC stays in the proximity of the capture-shrinkage IS_1, see Fig. 7 *i*, since the cortical-sliding dyneins pull the MTOC in different directions and oppose each other. Moreover, the MTOC is pulled back to the close IS by MTs occasionally attached to capture-shrinkage dyneins in the center of the IS_1, visually depicted by the red short MT in Fig. 6 *f*. Video S6 shows the process for $\gamma = \pi$ and $\rho^1_{IS} = \tilde{\rho}^2_{IS} = 1000\ \mu m^{-2}$.

The transition frequency decreases with the distance between the two IS when $\gamma \leq \frac{2\pi}{3}$, see Fig. 7 *a*, since the MTOC has to travel longer distance. When $\gamma > \frac{2\pi}{3}$ the distance is compensated by the increased attachment probability in the center of the IS caused by the increased probability density of MTs length corresponding to the circumferential distance between the two IS, see Fig. 2 *f*. An increased number of attached capture-shrinkage MTs leads to the decreased cortical-sliding dwelling times as the γ increases, see Fig. 7. The capture-shrinkage dwell times increase with γ, since the higher number of MTs pulls the MTOC closer to the IS, see Fig. 7, *f* and *i*.

Combined mechanisms in both IS

The time evolution of the cytoskeleton under the effect of both mechanisms with equal densities in both IS $\tilde{\rho}^1_{IS} = \tilde{\rho}^2_{IS} = \rho^1_{IS} = \rho^2_{IS} = 400\ \mu m^{-2}$, $\gamma = \frac{3\pi}{4}$, is shown in the Video S7. During the simulation, the MTOC repeatedly transitions between the two IS. The snapshots of one transition can be seen in Fig. 8. At the end of the transition, the MTs intersecting with the center of the distant IS are captured by dyneins, as visualized in Fig. 8 *a*. The cortical-sliding dyneins in the right IS have to compete with both mechanisms from the left IS and detach. Consequently, the MTOC is pulled to the left IS by both mechanisms and the movement is not opposed by the forces from the right IS, visualized in Fig. 8 *b*. As the MTOC approaches the left IS, capture-shrinkage MTs detach. Simultaneously, MTs are captured on the other side of the cell. Consequently, the stalk connecting the MTOC and the IS is formed and both mechanisms pull the MTOC to the right IS, as visualized in Fig. 8 *c*. As the MTOC approaches the right IS, dyneins of both mechanisms detach. Simultaneously, dyneins attach in the distant IS and initialize the next transition.

Fig. 8 *d* shows that the transition frequency increases with the dynein density. Moreover, the transition frequency decreases with the increasing angle γ only when $\gamma \leq \frac{3\pi}{4}$ and reaches the maximum when $\gamma = \pi$. Surprisingly, dwell times in the proximity of the IS do not steadily decrease with the dynein density despite the continuous decrease of the time that the MTOC spends in one hemisphere, see Fig. 8 *e*. The dwell times decrease with the dynein density until they reach a minimum when $\rho \sim 400\ \mu m^{-2}$ and then slightly increase. The standard deviation of the polar angle slightly increases and decreases when $\gamma<\pi$ and $\gamma = \pi$, respectively.

By comparison between Figs. 4, *d–f* and 8, *g* and *h*, one realizes that the MTOC trajectories under the effects of both mechanisms follow the same pattern as in the case of the sole capture-shrinkage mechanism: the MTOC travels

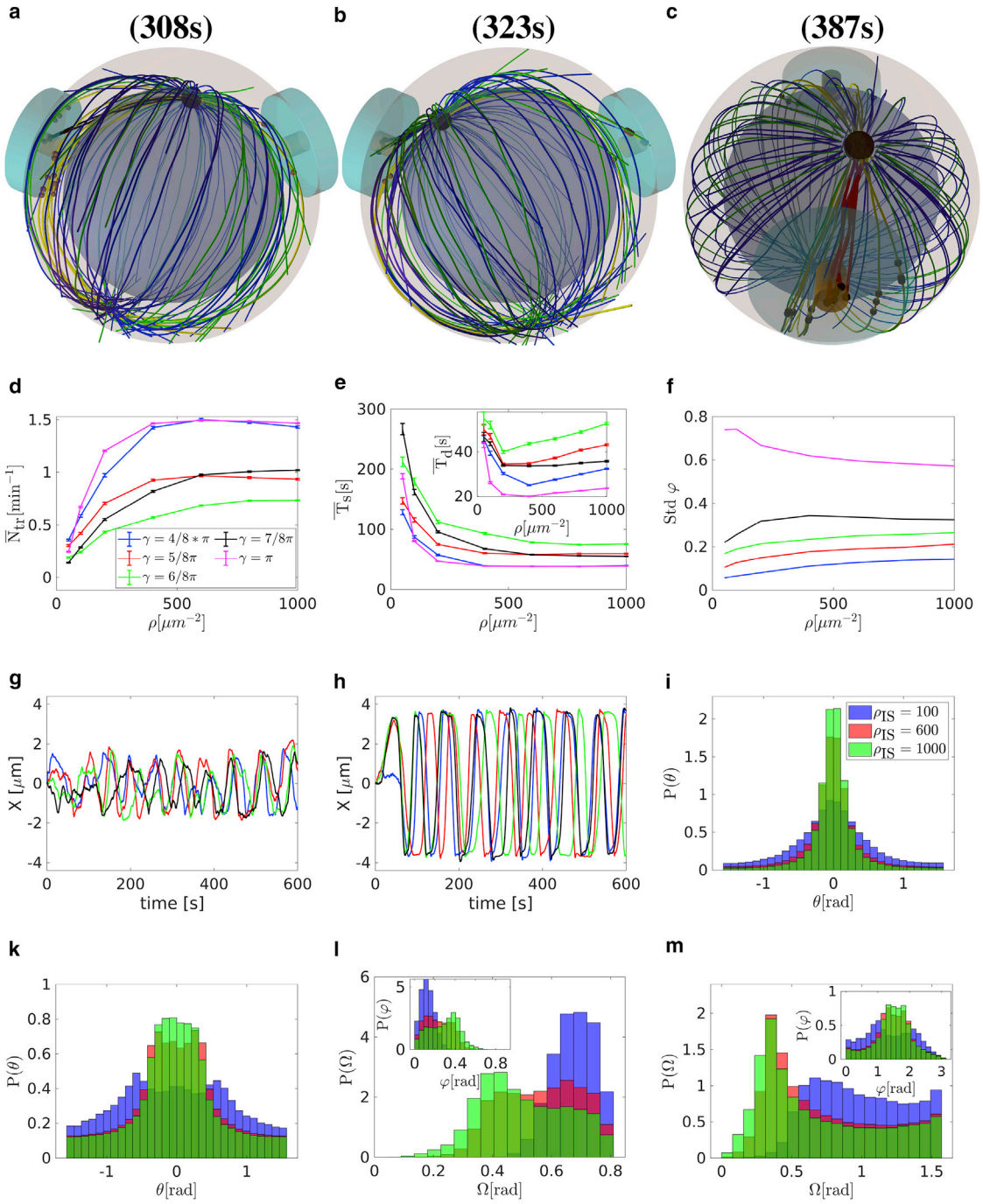

FIGURE 8 Combination of capture-shrinkage and cortical-sliding mechanisms with the same dynein density in both IS, $\tilde{\rho}^1_{IS} = \tilde{\rho}^2_{IS} = \rho^1_{IS} = \rho^2_{IS} = \rho$. (*a–c*) Snapshots from the time evolution of the MT cytoskeleton. $\rho = 400\ \mu m^{-2}$, $\gamma = \frac{3\pi}{4}$. Symbols and colors as in Fig. 2. (*a*) MTs intersecting with the center of the left IS attach to capture-shrinkage dyneins. Cortical-sliding dyneins attach to MTs at the periphery of both IS. (*b*) MTs captured in the left IS depolymerize as the MTOC approaches. Both capture-shrinkage and cortical-sliding MTs detach from dyneins. (*c*) Snapshot from the perspective of the right IS. MTs detached from the capture-shrinkage dyneins in the left IS. Simultaneously, MTs intersect with the center of the right IS and are captured by dyneins. Cortical-sliding dyneins attach at the right IS and detach at the left IS. (*d–f*) Dependencies of the average transition frequency $\overline{N}_{tr}$ (*d*), the time that the MTOC spends in one hemisphere $\overline{T}_s$ and the dwell time in the proximity of the IS $\overline{T}_d$ (*e*), and the standard deviation of the polar angle φ (*f*) on the dynein density ρ.(*d* and *e*) Dependencies are plotted with error bars. (*g* and *h*) Examples of the time evolution of the MTOC position in 600 s of simulation. The time evolutions of *x* coordinate of the MTOC are shown, $\rho = 600\ \mu m^{-2}$. (*g*) $\gamma = \frac{\pi}{2}$, (*h*) $\gamma = \pi$. (*I* and *k*) Probability distributions of the azimuthal angle θ. (*i*) $\gamma = \frac{\pi}{2}$, (*k*) $\gamma = \pi$. (*l* and *m*) Probability distributions of the angle Ω between the MTOC and the IS and the polar angle φ. (*l*) $\gamma = \frac{\pi}{2}$, (*m*) $\gamma = \pi$. To see this figure in color, go online.

TABLE 1 Synopsis of cortical sliding/capture shrinkage

	Capture shrinkage	Cortical sliding	Different mechanisms	Combined mechanisms
Transition frequencies N_{tr}	N_{tr} increases with ρ_{IS} and maximal for $\gamma = \pi$	N_{tr} decreases with γ, and $\tilde{\rho}_{IS}$ for $\gamma \geq \frac{2\pi}{3}$	N_{tr} increases with ρ; $\gamma<\pi$. N_{tr} depends non-monotonously on ρ for $\gamma \approx \pi$	N_{tr} increases with ρ, maximal for $\gamma = \pi$
Dwell times T_D	T_D decreases with ρ_{IS}	MTOC does not come close to one of the two IS for $\tilde{\rho}_{IS}<600\ \mu m^2$ and $\gamma<\frac{2\pi}{3}$, only fluctuates between the two hemispheres	T_D decreases and increases with ρ at the sliding, shrinkage IS, respectively	T_D decreases and then increases with ρ
Angles: azimuthal θ,Polar φ; MTOC-IS Ω	fluctuations of θ decrease with ρ_{IS} for $\gamma<\frac{2\pi}{3}$, but increase for $\gamma \approx \pi$	fluctuations of φ and Ω decrease for increasing $\tilde{\rho}_{IS}$ when $\gamma \approx \pi$	Ω decreases and MTOC is closer to shrinkage IS as ρ increases	fluctuations of φ increase with ρ, except when $\gamma \approx \pi$, when they decrease
MT cytoskeleton morphology	MTs form a stalk connecting the MTOC and the IS. Dyneins in IS can remain unattached for a time	MTs always intersect the IS. MTOC stays at one of the two IS for $\tilde{\rho}_{IS}>600\ \mu m^{-2}$	MT stalk connects MTOC and s hrinkage IS. Capture shrinkage becomes dominant as ρ increases	captured MTs shrink and detach. Sliding dynein acts on reduced number of MTs at close IS

to one IS, dwells in its close proximity, then transitions to the second IS. Moreover, the transitions between two IS are regular and continuous when $\gamma = \pi$ and incomplete and irregular when $\gamma = \frac{\pi}{2}$. As in the case of the capture-shrinkage mechanism, increasing circumferential distance between the two IS increases the probability that the plus-end of an MT is captured in the center of the distant IS due to the increasing probability density of MT length, see Fig. 2 *f*. Consequently, the dynein acts on an increased number of filaments as the γ increases, assuring continuous transition.

The combination of mechanisms leads to the unprecedented transition frequency and shortest dwell times, compare Figs. 4, 7, and 8. The reason is that the capture-shrinkage mechanism supports the cortical-sliding mechanism at the distant IS and hinders it at the close IS. At the end of the transitions, capture-shrinkage MTs are depolymerized and the cortical-sliding dyneins can attach to a lower number of MTs. Contrarily, MTs attach to the capture-shrinkage dyneins in the distant center and the two mechanisms pull in alignment sharing the load from opposing forces, as visualized in Fig. 8 *c*. Consequently, the MTOC is pulled to the distant IS by two mechanisms and to the close IS just by the cortical sliding acting on a reduced number of MTs.

The dwell times decrease with the rising dynein density, see Fig. 8 *e*, due to the higher pulling force. The slight increase of dwelling times when $\rho>400\ \mu m^{-2}$ is caused by the fact that the MTOC travels closer to the IS, see Fig. 8, *l* and *m*, and spends more time in the proximity of the IS. The monotonously decreasing times that the MTOC spends in one hemisphere indicate that the process gets faster with the dynein density despite the slightly increased dwelling times, see Fig. 8 *e*.

When $\gamma<\pi$, the standard deviation of the polar angle increases with the dynein density, see Fig. 8 *f*, because the MTOC is pulled closer to the IS and the angle has a wider range, see Fig. 8 *l*. The standard deviation of the polar angle is the largest when $\gamma = \pi$, since the MTOC can transition between IS through the lower hemisphere, sketched in Fig. 2 *b*. The standard deviation slightly decreases with the density. The reason lies in the fast speed of the MTOC transitions that leads to the fast transition from one IS to the second. Fig. 8 *m* shows that the MTOC is increasingly located closer to the IS when $\gamma = \pi$. The deviations from the *xz* plane decrease with the rising density, Fig. 8 *i* and *k*. The probability density does not have a peak at $\theta = 0$ when $\gamma = \pi$ at low densities, see Fig. 8 *k*, since the transitions pull the MTOC from the *xz* plane and the force is often insufficient to finish the transition in the close proximity of the IS center.

Synopsis of cortical sliding/capture shrinkage

Here, and in Table 1, we present a brief synopsis of the main differences that our model predicts when different mechanisms operate in both or in individual IS. When

only the cortical-sliding mechanism is acting, the transition frequency decreases with increasing angle γ, see Fig. S13 *a*. Contrarily to the capture-shrinkage mechanism, cortical-sliding dyneins are in a constant tug-of-war. When the dynein densities are small, the MTOC wiggles around the central position, see Fig. 5, *d*, *g*, and *j*. As the dynein density increases, one IS gains the upper hand and pulls the MTOC to the IS, see Fig. 5, *f*, *I*, and *l*. A subsequent transition to the distant IS is unlikely, since the dyneins from the distant IS have to overcome the forces from the close IS and the forces from the nucleus increasing with γ.

The mechanisms can be compared by locating them in different IS. One observes that for $\rho_{IS}<600\ \mu m^{-2}$, the average angle between the MTOC and the capture-shrinkage IS_1 $\overline{\Omega}>\frac{\gamma}{2}$, indicating that the MTOC is located closer to the cortical-sliding IS_2, see Fig. 7 *b*. As the density increases, the capture-shrinkage mechanism gains the upper hand and the MTOC is located closer to the capture-shrinkage IS_1, see Fig. 7, *b*, *f*, and *i*. One can therefore conclude that the cortical-sliding mechanism is stronger only when $\rho_{IS}<600\ \mu m^{-2}$ and weaker otherwise. When $\gamma = \pi$, the transition frequency decreases with increasing dynein density when $\rho_{IS}>400\ \mu m^{-2}$. As the dynein density increases the MTOC moves closer to the IS and dwells there, since cortical-sliding dyneins act against each other, as visualized in Fig. 6 *f*.

When the two mechanisms act together in both IS, the transition frequency is the highest and the dwell times are the lowest. The high transition frequency is due to the fact that as the MTOC is located in the proximity of one IS; the two mechanisms work together in the distant IS and oppose each other at the closer IS. As the MTOC approaches the IS, the captured MTs depolymerize and at the end detach from dyneins. Consequently, the capture-shrinkage mechanism cannot keep the MTOC at the close IS and the cortical-sliding mechanism acts on a reduced number of MTs. On the other hand, the dyneins from both mechanisms cooperate at the distant IS and share the load from opposing forces, reducing their detachment rate.

Surprisingly, when only the capture-shrinkage mechanism is acting, the transition frequency slightly decreases with increasing angle γ for $\gamma \leq \frac{2\pi}{3}$ and increases otherwise, see Fig. 4. This behavior can be explained by the shape of the MT length distribution, see Fig. 2 *f*. As the angle γ increases, increasing numbers of MTs have a length corresponding to the circumferential distance between two IS. Increasing numbers of attached MTs result in stronger pulling forces as well as higher transition frequency and smaller dwelling times.

DISCUSSION

The cell can polarize with stunning efficiency by employing two mechanisms performing differently in various cell configurations. In our computational model, the synergy of the two mechanisms manifests itself in reduced relocation times. In a real cell where the cytoskeleton is dragged through the inhomogeneous environment of organelles and filaments, the synergy can make a difference between complete and unfinished repositioning. Thus it appears that the location of dyneins on the IS periphery and the combination of two synergetically acting mechanisms together form a complex, efficient machinery, ensuring that the crucial immune response of human body is carried out efficiently while saving resources.

In situations in which the T cell has two IS, several scenarios have been observed experimentally (15) and are also predicted by our model: the MTOC alternates stochastically (but with a well-defined average transition time) between the two IS; it wiggles in between the two IS without transiting to one of the two; or it is at some point pulled to one of the two IS and stays there. We have analyzed with the help of our model which scenario emerges in dependency of the mechanisms in action and the number of dyneins present.

The emerging behavior of the MTOC is simplest when in both IS only the capture-shrinkage mechanism is acting: the frequency of transitions between the two IS increases monotonously with increasing ρ_{IS} and the dwell time at an IS decreases. The longitudinal fluctuations, described by the polar angle φ, also decrease with increasing ρ_{IS}, which means that the MTOC transits without much back and forth movement to the other IS when the dynein density is large. On the other hand, the transverse fluctuations do not depend significantly on ρ_{IS}. This nearly deterministic oscillatory behavior of the MTOC position is based on the presence of a mechanism detaching the pulling dyneins due to strong bending forces acting on the MT when the MTOC gets close to the center of an IS, cf. Fig. 2 *d*.

The situation becomes more complex as soon as cortical sliding plays a role, either in both IS or in one. If it is present in both, i.e., cortical sliding only, at both IS many MTs can attach to dynein and the resulting attached dynein populations are in a persistent tug-of-war, leading to stochastic alternations between the two hemispheres of the cell but without ever reaching the center of one IS. Except for very high dynein densities, when one IS can have a sufficiently strong, stochastic majority of attached dyneins it pulls the MTOC toward it and keeps it there, since no mechanism forcing the dyneins to detach is present in cortical sliding. Therefore, our model predicts that capture shrinkage is necessary to decide the tug-of-war that arises when two IS with low to medium dynein densities are present. In addition it predicts that when both mechanisms are present they can act even synergetically, since their cooperation results in the largest number of transitions. This observation suggests that the combination of the two mechanisms, capture shrinkage and cortical sliding, would actually allow the cell to kill two targets simultaneously.

Our results suggest that one may obtain insight into intracellular processes based on basic observations of the MTOC dynamics and cytoskeleton morphology. Regardless of the

number of the IS, the stalk of MTs sprouting from the MTOC and ending in the center of the IS is indicative of the capture-shrinkage mechanism. Its presence is also suggested by uninterrupted transitions and small dwelling times. Incomplete, interrupted transitions at small angle γ and long dwelling at one IS when $\gamma \geq \frac{2\pi}{3}$ are characteristic of the cortical-sliding mechanism. Moreover, the MTOC dynamics in the cell with two IS may offer a way to estimate the MT length distribution. Since the number of transitions does not decrease with increasing distance between the two IS and it is maximal when the distance corresponds to the peak of the length distribution, the experimental observations of the repositioning in the cell with two IS in different configurations may suggest the distribution of MT lengths.

In conclusion, we provided here a fairly complete picture of MTOC repositioning with one or two IS, under the model assumption of a fixed (spherical) cell shape. It would certainly be rewarding to include a deformable, semiflexible (due to the actin cortex) cell boundary interacting mechanically with the forces exerted by the semiflexible MTs. Another open question concerns the way in which dyneins are spatially organized in the membrane: do they self-organize (42,78,112) or are they more or less firmly anchored in the actin cortex, as we assumed in our model? Probably more experimental insight is necessary to decide this question.

From a broader perspective, MTOC/centrosome precise positioning is also crucial for other cell functions: in addition to the polarized immune response of lymphocytes considered here, it also determines either the axis of cell division or the direction of cell migration (113). In the latter contexts the centrosome is subjected to a force field of pulling and pushing forces that are mediated by cortical dynein and centrosome nucleated MTs, respectively. Our model included mainly pulling forces, as centrosome positioning in T cells is largely dependent on dynein, but a recent study (114) indicated that myosin-mediated pushing forces might also play a role in this process: dynein and myosin II accumulate at opposite cell poles following IS formation. While the dynein-dependent mechanism generates pulling forces at the IS, the asymmetric distribution of non-muscle myosin creates pushing forces from the opposite pole. Possibly the last phase of MTOC repositioning, the slow final approach toward the IS, is supported by these pushing forces—a hypothesis that could quantitatively be tested by our model, augmented also by an elastic and spatially inhomogeneous active cell boundary.

SUPPORTING MATERIAL

Supporting material (Vodeps S8–S10) can be found online at https://doi.org/10.1016/j.bpj.2022.02.029.

AUTHOR CONTRIBUTIONS

I.H. and H.R. designed the research. I.H. performed calculations, prepared figures, and analyzed the data. I.H. and H.R. wrote the manuscript.

ACKNOWLEDGMENTS

This work was financially supported by the German Research Foundation (DFG) within the Collaborative Research Center SFB 1027.

REFERENCES

1. Rudolph, M. G., R. L. Stanfield, and I. A. Wilson. 2006. How TCRs bind MHCs, peptides, and coreceptors. *Annu. Rev. Immunol.* 24:419–466.
2. Garcia, K. C. 2012. Reconciling views on T cell receptor germline bias for MHC. *Trends Immunol.* 33:429–436.
3. Zinkernagel, R. M., and P. C. Doherty. 1974. Restriction of *in vitro* T cell-mediated cytotoxicity in lymphocytic choriomeningitis within a syngeneic or semiallogeneic system. *Nature.* 248:701.
4. Attaf, M., M. Legut, …, A. K. Sewell. 2015. The T cell antigen receptor: the Swiss army knife of the immune system. *Clin. Exp. Immunol.* 181:1–18.
5. Wucherpfennig, K. W. 2004. T cell receptor crossreactivity as a general property of T cell recognition. *Mol. Immunol.* 40:1009–1017.
6. Babbitt, B. P., P. M. Allen, …, E. R. Unanue. 1985. Binding of immunogenic peptides to Ia histocompatibility molecules. *Nature.* 317:359.
7. Monks, C. R., B. A. Freiberg, …, A. Kupfer. 1998. Three-dimensional segregation of supramolecular activation clusters in T cells. *Nature.* 395:82–86.
8. Dustin, M. L., M. W. Olszowy, …, A. S. Shaw. 1998. A novel adaptor protein orchestrates receptor patterning and cytoskeletal polarity in T-cell contacts. *Cell.* 94:667–677.
9. Dustin, M. L., A. K. Chakraborty, and A. S. Shaw. 2010. Understanding the structure and function of the immunological synapse. *Cold Spring Harb Perspect. Biol.* 2:a002311.
10. Geiger, B., D. Rosen, and G. Berke. 1982. Spatial relationships of microtubule-organizing centers and the contact area of cytotoxic T lymphocytes and target cells. *J. Cell Biol.* 95:137–143.
11. Kupfer, A., D. Louvard, and S. J. Singer. 1982. Polarization of the Golgi apparatus and the microtubule-organizing center in cultured fibroblasts at the edge of an experimental wound. *Proc. Natl. Acad. Sci. U S A.* 79:2603–2607.
12. Yi, J., X. Wu, …, J. A. Hammer. 2013. Centrosome repositioning in T cells is biphasic and driven by microtubule end-on capture-shrinkage. *J. Cell Biol.* 202:779–792.
13. Stinchcombe, J. C., E. Majorovits, …, G. M. Griffiths. 2006. Centrosome polarization delivers secretory granules to the immunological synapse. *Nature.* 443:462–465.
14. Maccari, I., R. Zhao, …, H. Rieger. 2016. Cytoskeleton rotation relocates mitochondria to the immunological synapse and increases calcium signals. *Cell Calcium.* 60:309–321.
15. Kuhn, J. R., and M. Poenie. 2002. Dynamic polarization of the microtubule cytoskeleton during CTL-mediated killing. *Immunity.* 16:111–121.
16. Hui, K. L., and A. Upadhyaya. 2017. Dynamic microtubules regulate cellular contractility during T-cell activation. *Proc. Natl. Acad. Sci. U S A.* 114:E4175–E4183.
17. Kupfer, A., and G. Dennert. 1984. Reorientation of the microtubule-organizing center and the Golgi apparatus in cloned cytotoxic lymphocytes triggered by binding to lysable target cells. *J. Immunol.* 133:2762–2766.
18. Kupfer, A., S. L. Swain, …, S. J. Singer. 1986. The specific direct interaction of helper T cells and antigen-presenting B cells. *Proc. Natl. Acad. Sci. U S A.* 83:6080–6083.
19. Gurel, P., A. Hatch, and H. Higgs. 2014. Connecting the cytoskeleton to the endoplasmic reticulum and Golgi. *Curr. Biol.* 24:R660–R672.
20. Lee, C., and L. B. Chen. 1988. Dynamic behavior of endoplasmic reticulum in living cells. *Cell.* 54:37–46.

21. Waterman-Storer, C. M., and E. D. Salmon. 1998. Endoplasmic reticulum membrane tubules are distributed by microtubules in living cells using three distinct mechanisms. *Curr. Biol.* 8:798–806.
22. Palmer, K. J., P. Watson, and D. J. Stephens. 2005. The role of microtubules in transport between the endoplasmic reticulum and Golgi apparatus in mammalian cells. *Biochem. Soc. Symp.* 72:1–13.
23. Müllbacher, A., P. Waring, …, M. M. Simon. 1999. Granzymes are the essential downstream effector molecules for the control of primary virus infections by cytolytic leukocytes. *PNAS.* 96:13950–13955.
24. Lowin, B., M. C. Peitsch, and J. Tschopp. 1995. Perforin and granzymes: crucial effector molecules in cytolytic T lymphocyte and natural killer cell-mediated cytotoxicity. *Curr. Top. Microbiol. Immunol.* 198:1–24.
25. Voskoboinik, I., M. J. Smyth, and J. A. Trapani. 2006. Perforin-mediated target-cell death and immune homeostasis. *Nat. Rev. Immunol.* 6:940–952.
26. Grossman, W. J., P. A. Revell, …, T. J. Ley. 2003. The orphan granzymes of humans and mice. *Curr. Opin. Immunol.* 15:544–552.
27. Krzewski, K., and J. E. Coligan. 2012. Human NK cell lytic granules and regulation of their exocytosis. *Front. Immunol.* 3:335.
28. Groscurth, P., and L. Filgueira. 1998. Killing mechanisms of cytotoxic T lymphocytes. *Physiology.* 13:17–21.
29. Golstein, P., and G. M. Griffiths. 2018. An early history of T cell-mediated cytotoxicity. *Nat. Rev. Immunol.* 18:527–535.
30. Bertrand, F., S. Müller, …, S. Valitutti. 2013. An initial and rapid step of lytic granule secretion precedes microtubule organizing center polarization at the cytotoxic T lymphocyte/target cell synapse. *Proc. Natl. Acad. Sci. U.S.A.* 110:6073–6078.
31. Andre, P., A. M. Benoliel, …, P. Bongrand. 1990. Use of conjugates made between a cytolytic T cell clone and target cells to study the redistribution of membrane molecules in cell contact areas. *J. Cell Sci.* 97:335–347.
32. Lin, J., M. J. Miller, and A. S. Shaw. 2005. The c-SMAC. *J. Cell Biol.* 170:177–182.
33. Choudhuri, K., and M. L. Dustin. 2010. Signaling microdomains in T cells. *FEBS Lett.* 584:4823–4831.
34. Martín-Cófreces, N. B., J. Robles-Valero, …, F. Sánchez-Madrid. 2008. MTOC translocation modulates IS formation and controls sustained T cell signaling. *J. Cell Biol.* 182:951–962.
35. Nguyen-Ngoc, T., K. Afshar, and P. Gönczy. 2007. Coupling of cortical dynein and Gα proteins mediates spindle positioning in *Caenorhabditis elegans*. *Nat. Cell Biol.* 9:1294–1302.
36. Saito, T. T., D. Okuzaki, and H. Nojima. 2006. Mcp5, a meiotic cell cortex protein, is required for nuclear movement mediated by dynein and microtubules in fission yeast. *J. Cell Biol.* 173:27–33.
37. Yamashita, A., and M. Yamamoto. 2006. Fission yeast Num1p is a cortical factor Anchoring dynein and is essential for the horse-tail nuclear movement during meiotic prophase. *Genetics.* 173:1187–1196.
38. Ananthanarayanan, V., M. Schattat, …, I. M. Tolić-Nørrelykke. 2013. Dynein motion switches from diffusive to directed upon cortical anchoring. *Cell.* 153:1526–1536.
39. Combs, J., S. J. Kim, …, M. Poenie. 2006. Recruitment of dynein to the Jurkat immunological synapse. *Proc. Natl. Acad. Sci. U.S.A.* 103:14883–14888.
40. Hashimoto-Tane, A., T. Yokosuka, …, T. Saito. 2011. Dynein-driven transport of T cell receptor microclusters regulates immune synapse formation and T cell activation. *Immunity.* 34:919–931.
41. Stinchcombe, J. C., and G. M. Griffiths. 2014. Communication, the centrosome and the immunological synapse. *Philos. Trans. R. Soc. Lond. B Biol. Sci.* 369:20130463.
42. Sanchez, E., X. Liu, and M. Huse. 2019. Actin clearance promotes polarized dynein accumulation at the immunological synapse. *PLoS One.* 14:e0210377.
43. Laan, L., N. Pavin, …, M. Dogterom. 2012. Cortical dynein controls microtubule dynamics to generate pulling forces that position microtubule asters. *Cell.* 148:502–514.
44. Grill, S. W., K. Kruse, and F. Jülicher. 2005. Theory of mitotic spindle oscillations. *Phys. Rev. Lett.* 94:108104.
45. Kozlowski, C., M. Srayko, and F. Nedelec. 2007. Cortical microtubule contacts position the spindle in C. elegans embryos. *Cell.* 129:499–510.
46. Grill, S. W., and A. A. Hyman. 2005. Spindle positioning by cortical pulling forces. *Dev. Cell.* 8:461–465.
47. Kruse, K., and F. Jülicher. 2005. Oscillations in cell biology. *Curr. Opin. Cell Biol.* 17:20–26.
48. Colombo, K., S. W. Grill, …, P. Gönczy. 2003. Translation of polarity cues into asymmetric spindle positioning in Caenorhabditis elegans embryos. *Science.* 300:1957–1961.
49. Grill, S. W., J. Howard, …, A. A. Hyman. 2003. The distribution of active force generators controls mitotic spindle position. *Science.* 301:518–521.
50. Grill, S. W., P. Gönczy, …, A. A. Hyman. 2001. Polarity controls forces governing asymmetric spindle positioning in the Caenorhabditis elegans embryo. *Nature.* 409:630–633.
51. Siller, K. H., and C. Q. Doe. 2009. Spindle orientation during asymmetric cell division. *Nat. Cell Biol.* 11:365–374.
52. Couwenbergs, C., J.-C. Labbé, …, M. Gotta. 2007. Heterotrimeric G protein signaling functions with dynein to promote spindle positioning in C. elegans. *J. Cell Biol.* 179:15–22.
53. Pecreaux, J., J.-C. Röper, …, J. Howard. 2006. Spindle oscillations during asymmetric cell division require a threshold number of active cortical force generators. *Curr. Biol.* 16:2111–2122.
54. Kim, M. J., and I. V. Maly. 2009. Deterministic mechanical model of T-killer cell polarization reproduces the wandering of aim between simultaneously engaged targets. *PLoS Comput. Biol.* 5:e1000260.
55. Vogel, S. K., N. Pavin, …, I. M. Tolić-Nørrelykke. 2009. Self-Organization of dynein motors generates meiotic nuclear oscillations. *PLoS Biol.* 7:e1000087.
56. Ding, D. Q., Y. Chikashige, …, Y. Hiraoka. 1998. Oscillatory nuclear movement in fission yeast meiotic prophase is driven by astral microtubules, as revealed by continuous observation of chromosomes and microtubules in living cells. *J. Cell Sci.* 111 (Pt 6):701–712.
57. Yamamoto, A., R. R. West, …, Y. Hiraoka. 1999. A cytoplasmic dynein heavy chain is required for oscillatory nuclear movement of meiotic prophase and efficient meiotic recombination in fission yeast. *J. Cell Biol.* 145:1233–1249.
58. Walker, R. A., E. T. O'Brien, …, E. D. Salmon. 1988. Dynamic instability of individual microtubules analyzed by video light microscopy: rate constants and transition frequencies. *J. Cell Biol.* 107:1437–1448.
59. Mitchison, T., and M. Kirschner. 1984. Dynamic instability of microtubule growth. *Nature.* 312:237–242.
60. Vorob'ev, I. A., and I. S. Grigor'ev. 2003. Dynamics and the life cycle of cell microtubules). *Tsitol Genet.* 37:22–38.
61. Horio, T., and T. Murata. 2014. The role of dynamic instability in microtubule organization. *Front. Plant Sci.* 5:511.
62. Brouhard, G. J. 2015. Dynamic instability 30 years later: complexities in microtubule growth and catastrophe. *Mol. Biol. Cell.* 26:1207–1210.
63. Mandelkow, E. M., E. Mandelkow, and R. A. Milligan. 1991. Microtubule dynamics and microtubule caps: a time-resolved cryo-electron microscopy study. *J. Cell Biol.* 114:977–991.
64. Bieling, P., L. Laan, …, T. Surrey. 2007. Reconstitution of a microtubule plus-end tracking system *in vitro*. *Nature.* 450:1100–1105.
65. Desai, A., and T. J. Mitchison. 1997. Microtubule polymerization dynamics. *Annu. Rev. Cell Dev. Biol.* 13:83–117.
66. Kerssemakers, J. W. J., E. Laura Munteanu, …, M. Dogterom. 2006. Assembly dynamics of microtubules at molecular resolution. *Nature.* 442:709–712.

67. Schek, H. T., M. K. Gardner, …, A. J. Hunt. 2007. Microtubule assembly dynamics at the nanoscale. *Curr. Biol.* 17:1445–1455.

68. Gardner, M. K., A. J. Hunt, …, D. J. Odde. 2008. Microtubule assembly dynamics: new insights at the nanoscale. *Curr. Opin. Cell Biol.* 20:64–70.

69. Myers, K. A., K. T. Applegate, …, C. M. Waterman. 2011. Distinct ECM mechanosensing pathways regulate microtubule dynamics to control endothelial cell branching morphogenesis. *J. Cell Biol.* 192:321–334.

70. Lacroix, B., G. Letort, …, J. Dumont. 2018. Microtubule dynamics scale with cell size to set spindle length and assembly timing. *Dev. Cell.* 45:496–511.e6.

71. Fuesler, J., and H.-J. Li. 2012. Dynamic instability – a common denominator in prokaryotic and eukaryotic DNA segregation and cell division. *Cell Mol. Biol. Lett.* 17:542–548.

72. Hornak, I., and H. Rieger. 2020. Stochastic model of T cell repolarization during target elimination I. *Biophys. J.* 118:1733–1748.

73. Wu, H.-Y., E. Nazockdast, …, D. J. Needleman. 2017. Forces positioning the mitotic spindle: theories, and now experiments. *BioEssays.* 39:1600212.

74. Garzon-Coral, C., H. A. Fantana, and J. Howard. 2016. A force-generating machinery maintains the spindle at the cell center during mitosis. *Science.* 352:1124–1127.

75. Howard, J. 2006. Elastic and damping forces generated by confined arrays of dynamic microtubules. *Phys. Biol.* 3:54–66.

76. Pécréaux, J., S. Redemann, …, J. Howard. 2016. The mitotic spindle in the one-cell C. elegans embryo is positioned with high precision and stability. *Biophys. J.* 111:1773–1784.

77. Dogterom, M., and B. Yurke. 1997. Measurement of the force-velocity relation for growing microtubules. *Science.* 278:856–860.

78. Gros, O. J., H. G. J. Damstra, …, F. Berger. 2021. Dynein self-organizes while translocating the centrosome in T-cells. *MBoC.* 32:855–868.

79. Zhang, R., G. Alushin, …, E. Nogales. 2015. Mechanistic origin of microtubule dynamic instability and its modulation by EB proteins. *Cell.* 162:849–859.

80. Cassimeris, L., N. K. Pryer, and E. D. Salmon. 1988. Real-time observations of microtubule dynamic instability in living cells. *J. Cell Biol.* 107:2223–2231.

81. Sammak, P. J., and G. G. Borisy. 1988. Direct observation of microtubule dynamics in living cells. *Nature.* 332:724–726.

82. Belmont, L. D., A. A. Hyman, …, T. J. Mitchison. 1990. Real-time visualization of cell cycle-dependent changes in microtubule dynamics in cytoplasmic extracts. *Cell.* 62:579–589.

83. Zwetsloot, A., G. Tut, and A. Straube. 2018. Measuring microtubule dynamics. *Essays Biochem.* 62:725–735.

84. Steinberg, G., R. Wedlich-Soldner, …, I. Schulz. 2001. Microtubules in the fungal pathogen Ustilago maydis are highly dynamic and determine cell polarity. *J. Cell Sci.* 114:609–622.

85. Yvon, A. M., and P. Wadsworth. 1997. Non-centrosomal microtubule formation and measurement of minus end microtubule dynamics in A498 cells. *J. Cell Sci.* 110:2391–2401.

86. Carminati, J. L., and T. Stearns. 1997. Microtubules orient the mitotic spindle in yeast through dynein-dependent interactions with the cell cortex. *J. Cell Biol.* 138:629–641.

87. Adames, N. R., and J. A. Cooper. 2000. Microtubule interactions with the cell cortex causing nuclear movements in Saccharomyces cerevisiae. *J. Cell Biol.* 149:863–874.

88. Drummond, D. R., and R. A. Cross. 2000. Dynamics of interphase microtubules in Schizosaccharomyces pombe. *Curr. Biol.* 10:766–775.

89. Van Damme, D., K. Van Poucke, …, D. Geelen. 2004. *In vivo* dynamics and differential microtubule-binding activities of MAP65 proteins. *Plant Physiol.* 136:3956–3967.

90. Yamashita, N., M. Morita, …, Y. Mimori-Kiyosue. 2015. Three-dimensional tracking of plus-tips by lattice light-sheet microscopy permits the quantification of microtubule growth trajectories within the mitotic apparatus. *JBO.* 20:101206.

91. Tirnauer, J. S., E. O'Toole, …, D. Pellman. 1999. Yeast Bim1p promotes the G1-specific dynamics of microtubules. *J. Cell Biol.* 145:993–1007.

92. Komarova, Y. A., I. A. Vorobjev, and G. G. Borisy. 2002. Life cycle of MTs: persistent growth in the cell interior, asymmetric transition frequencies and effects of the cell boundary. *J. Cell Sci.* 115:3527–3539.

93. Alieva, I. B., E. A. Zemskov, …, A. D. Verin. 2010. Microtubules growth rate alteration in human endothelial cells. *J. Biomed. Biotechnol.* 2010:671536.

94. Brunner, D., and P. Nurse. 2000. CLIP170-like tip1p spatially organizes microtubular dynamics in fission yeast. *Cell.* 102:695–704.

95. Rusan, N. M., C. J. Fagerstrom, …, P. Wadsworth. 2001. Cell cycle-dependent changes in microtubule dynamics in living cells expressing green fluorescent protein- α tubulin. *Mol. Biol. Cell.* 12:971–980.

96. Trushko, A., E. Schäffer, and J. Howard. 2013. The growth speed of microtubules with XMAP215-coated beads coupled to their ends is increased by tensile force. *PNAS.* 110:14670–14675.

97. Shelden, E., and P. Wadsworth. 1993. Observation and quantification of individual microtubule behavior *in vivo*: microtubule dynamics are cell-type specific. *J. Cell Biol.* 120:935–945.

98. Fees, C. P., and J. K. Moore. 2019. A unified model for microtubule rescue. *MBoC.* 30:753–765.

99. Tischer, C., D. Brunner, and M. Dogterom. 2009. Force- and kinesin-8-dependent effects in the spatial regulation of fission yeast microtubule dynamics. *Mol. Syst. Biol.* 5:250.

100. Ihornak - Overview. https://github.com/ihornak.

101. Quann, E. J., E. Merino, …, M. Huse. 2009. Localized diacylglycerol drives the polarization of the microtubule-organizing center in T cells. *Nat. Immunol.* 10:627–635.

102. Howard, J. 2001. Mechanics of Motor Proteins and the Cytoskeleton, new edition. Sinauer Associates.

103. Xu, H., W. Su, …, H. Wang. 2013. The asymmetrical structure of Golgi apparatus membranes revealed by *in situ* atomic force microscope. *PLoS One.* 8:e61596.

104. Ladinsky, M. S., D. N. Mastronarde, …, L. A. Staehelin. 1999. Golgi structure in three dimensions: functional insights from the normal rat kidney cell. *J. Cell Biol.* 144:1135–1149.

105. Day, K. J., L. A. Staehelin, and B. S. Glick. 2013. A three-stage model of Golgi structure and function. *Histochem. Cell Biol.* 140:239–249.

106. Huang, S., and Y. Wang. 2017. Golgi structure formation, function, and post-translational modifications in mammalian cells. *F1000Res.* 6:2050.

107. Westrate, L. M., J. E. Lee, …, G. K. Voeltz. 2015. Form follows function: the importance of endoplasmic reticulum shape. *Annu. Rev. Biochem.* 84:791–811.

108. English, A. R., and G. K. Voeltz. 2013. Endoplasmic reticulum structure and interconnections with other organelles. *Cold Spring Harb Perspect. Biol.* 5:a013227.

109. English, A. R., N. Zurek, and G. K. Voeltz. 2009. Peripheral ER structure and function. *Curr. Opin. Cell Biol.* 21:596–602.

110. Shibata, Y., G. K. Voeltz, and T. A. Rapoport. 2006. Rough sheets and smooth tubules. *Cell.* 126:435–439.

111. Hu, J., W. A. Prinz, and T. A. Rapoport. 2011. Weaving the web of ER tubules. *Cell.* 147:1226–1231.

112. Hooikaas, P. J., H. G. Damstra, …, A. Akhmanova. 2020. Kinesin-4 KIF21B limits microtubule growth to allow rapid centrosome polarization in T cells. *eLife.* 9:e62876.

113. Elric, J., and S. Etienne-Manneville. 2014. Centrosome positioning in polarized cells: common themes and variations. *Exp. Cell Res.* 328:240–248.

114. Liu, X., T. M. Kapoor, …, M. Huse. 2013. Diacylglycerol promotes centrosome polarization in T cells via reciprocal localization of dynein and myosin II. *Proc. Natl. Acad. Sci. U S A.* 110:11976–11981.